Evidence from achondrites for a temporal change in Nd nucleosynthetic anomalies within the first 1.5 million years of the inner solar system formation

P. Frossard, Zhiguo Guo, Mary Spencer, Maud Boyet, Audrey Bouvier

HAL Id: hal-03228316
https://uca.hal.science/hal-03228316

Submitted on 18 May 2021

Evidence from achondrites for a temporal change in Nd nucleosynthetic anomalies within the first 1.5 million years of the inner solar system formation

Paul Frossard[1,*], Zhiguo Guo[2], Mary Spencer[2], Maud Boyet[1], Audrey Bouvier[3, 2]

[1] Université Clermont Auvergne, CNRS, IRD, OPGC, Laboratoire Magmas et Volcans, F-63000 Clermont-Ferrand, France

[2] Department of Earth Sciences, University of Western Ontario, N6A 5B7 London, Ontario, Canada

[3] Bayerisches Geoinstitut, Universität Bayreuth, 95447 Bayreuth, Germany

*Corresponding author: paul.frossard@uca.fr

Abstract

Heterogeneity in isotopic compositions within the protoplanetary disc has been demonstrated for a number of elements measured in extra-terrestrial materials, mostly based on chondrite meteorite analyses. However, precise ^{182}Hf-^{182}W and ^{26}Al-^{26}Mg ages of iron meteorites, achondrites, and chondrules show that chondrites accreted later than achondrites and therefore do not strictly represent the early (< 2 Ma) solar system composition. Here we present the Nd mass-independent stable isotopic compositions of a suite of diverse achondrites to better constrain the Nd isotope evolution of the early solar system. Carbonaceous (C) achondrites are indistinguishable from their chondritic counterpart. However, early formed planetesimals as sampled by silicate-rich non-carbonaceous (NC) achondrite meteorites have higher ^{145}Nd/^{144}Nd and ^{148}Nd/^{144}Nd ratios (3.9 < μ^{145}Nd < 11.0 and 9.1 < μ^{148}Nd < 17.9 in part per million deviation, or μ^iNd) compared to NC chondrites (2.7 < μ^{145}Nd < 3.3 and 2.2 < μ^{148}Nd < 8.1). Moreover, the three terrestrial planets for which we have samples available (Earth, Mars, and the Moon) as well as the silicate inclusions from the non-magmatic IIE iron meteorite Miles present a systematic deficit in μ^{145}Nd and μ^{148}Nd compared to early-formed NC achondrites. Unlike chondrites, the Nd anomalies in achondrites are not correlated to the heliocentric distance of accretion of their respective parent bodies as inferred from redox conditions. Chronological constraints on planetesimal accretion suggests that Nd (and other elements such as Mo and Zr) nucleosynthetic compositions of the inner part of the protoplanetary disc significantly changed around 1.5 Ma after Solar System formation due to thermal processing of dust in the protoplanetary disc. This relatively late event coincides with the beginning of chondrule formation or at least their preservation. Terrestrial planets formed subsequently by a complex accretion regime during several million years. Therefore, two scenarios are envisioned considering the reported Nd isotope composition of early planetesimals: 1) Terrestrial planets accreted mostly chondritic material similar in composition to enstatite chondrites, or 2) early planetesimals constitute substantial parts of terrestrial planets building blocks mixed with highly thermally processed material enriched in *s*-process, still unsampled by meteorites.

Keywords: Nd nucleosynthetic anomalies, achondrites, planetesimals, chondrule formation, thermal processing

1. Introduction

The location and timing of planetesimal formation within the protoplanetary disc are two critical parameters that influenced the formation of the terrestrial planets (Earth, Mars, Venus, and Mercury) and the precursor of the Moon. Recent studies have found evidence for the coexistence of two isotopically distinct reservoirs: the non-carbonaceous (NC), and carbonaceous reservoirs (C) (Trinquier et al., 2007; Leya et al., 2008; Kruijer et al., 2017). Molybdenum and Hf-W systematics bear evidence for an early formation of non-carbonaceous and carbonaceous reservoirs before the accretion of differentiated (iron and achondrite meteorites) and undifferentiated (chondrites) planetesimals (Kruijer et al., 2017). The formation of Jupiter was proposed to have taken place within 1 million years after CAIs to explain the separation of these two isotopically distinct reservoirs (Kruijer et al., 2017). The parent bodies of the carbonaceous chondrites and achondrites may have formed within a distinct reservoir further out in the disc before being transferred with the NC parent bodies to form together the asteroid belt (Kruijer et al., 2020). Based on mass-independent isotopic anomalies of refractory (e.g., ^{50}Ti, ^{48}Ca) and non-refractory (e.g., ^{54}Cr, ^{58}Ni) elements, Earth appears systematically as an end-member for the Solar System inner nebular reservoir; the so-called NC reservoir (Mezger et al., 2020).

The formation timescales of differentiated planetesimals are constrained by the ^{182}Hf-^{182}W, ^{53}Mn-^{53}Cr and ^{26}Al-^{26}Mg radiometric ages and isotopic evolution models of achondrite meteorites (Sugiura and Fujiya, 2014). Achondrites can be samples of planetary cores (irons) and mantle and crust silicate layers (primitive achondrites and basaltic achondrites). We use the term achondrites hereafter to encompass silicate-rich meteorites from planetesimals. The crystallisation ages and geochemical compositions of achondrite meteorites together provide minimum ages for differentiation as well as model ages for the accretion of their respective parent bodies after CAIs. The parent bodies of most achondrites formed within the first 2 Ma after CAIs (based on ^{182}Hf-^{182}W, ^{26}Al-^{26}Mg model ages; e.g., Kruijer et al., 2017; Sugiura and Fujiya, 2014). In contrast, most chondrules from ordinary (LL, L) and carbonaceous chondrites (CV, CO, CM, CR), the main constituents of chondrites, formed from around 1.5 to 5 Ma after CAI based on ^{26}Al-^{26}Mg systematics (e.g., Pape et al., 2019). Consequently, the parent bodies of these chondrites must have accreted even later. Chondrites are generally used to define the building

blocks of the Earth. However, achondrites formed earlier, owing to the higher abundance of ^{26}Al at the time of formation of their parent body and may also contribute significantly to Earth's building blocks. Several studies have hinted at a possible temporal evolution of the inner protoplanetary disc composition and explained the latter by the incorporation of material of presolar (Sugiura and Fujiya, 2014) or CI chondrite nature (Schiller et al., 2018) into the accreting planetesimals.

The comparison of different systematics is complicated by the various carriers and behaviour of the elements. Therefore, cosmochemical interpretation of the protoplanetary disc evolution requires different processes to account for the variability of all systematics rather than a single process. Neodymium is interesting in this respect as it has six isotopes that are produced during stellar nucleosynthesis by *s*-, *r*- and *p*-processes in different proportions (Figure S1). Two isotopes, ^{142}Nd and ^{143}Nd, are produced in part by the radioactive decay of extinct ^{146}Sm and live ^{147}Sm for which the radiogenic contribution can blur the nucleosynthetic anomalies. Most notably, the difference between the ^{142}Nd/^{144}Nd ratio of chondrites and the Earth was originally attributed to an early differentiation event on Earth (Boyet and Carlson, 2005) before several studies show that nucleosynthetic anomalies are likely responsible for this offset (Bouvier and Boyet, 2016; Burkhardt et al., 2016). Nd nucleosynthetic anomalies, similarly to most heavy elements, are increasing from enstatite chondrites, through ordinary chondrites and finally carbonaceous chondrites. The distribution of Nd nucleosynthetic anomalies has been related to the heliocentric distance to account for the covariation of Nd and Mo in chondrites with Earth as an end-member, enriched in *s*-process as observed for many elements (Render et al., 2017). This led to the hypothesis that Earth formed from materials that are not present in our meteorite collections, although the closest match for the isotopic compositions of many elements are the enstatite chondrites (e.g. Akram et al., 2015; Burkhardt et al., 2016; Dauphas, 2017; Boyet et al., 2018). So far, very little high precision data is available on achondrites from the early planetesimals that probe the solar system composition before chondrule formation and terrestrial planets accretion.

In this study, we provide new Nd mass-independent isotope composition of achondrites from various groups from the NC and C reservoirs to assess the distribution of Nd nucleosynthetic anomalies within the protoplanetary disc over the first few million years of its existence. The ^{142}Nd/^{144}Nd and ^{143}Nd/^{144}Nd

are not discussed because of the uncertainties on corrections to make from radiogenic contributions owing to complex Sm/Nd fractionation histories for achondrites.

2. Methods

2.1 Samples

Fragments of one to three grams of 11 primitive and differentiated achondrite meteorites were obtained from national and private collections (see details in Supplementary Information). Achondrites from the newly defined non-carbonaceous and carbonaceous groups were selected for this study. Non-carbonaceous achondrites include two eucrites Tirhert and NWA 11001, ureilite Catalina 037; aubrite Khor Temiki; enstatite achondrite Itqiy (EH7); two ungrouped achondrites NWA 12338 (eucrite-like) and NWA 11119, as well as an individual silicate inclusion extracted from the IIE iron Miles. Two different fractions were analysed for NWA 11119, a whole-rock powder and a mixed fraction of mineral separates (pyroxene, plagioclase and silica). The two ungrouped carbonaceous achondrites analysed in this study are NWA 6704 and Tafassasset. In addition, the martian polymict breccia NWA 7034 was analysed.

2.2 Preparation and chemical procedure

Sample preparation, dissolution, and first stages of chemistry were carried out in cleanroom conditions in the GEOMETRIC laboratory at University of Western Ontario. The Sm and Nd final purification procedures were carried out at Laboratoire Magmas et Volcans (LMV). All chemicals were distilled in Savillex Teflon stills (HNO_3 and HCl) or purchased (HF, H_2O_2, $HClO_4$) at ppt levels or better for trace metals. Water was deionized using filtration systems to reach 18.2 MΩ resistivity.

All meteorite fragments were first cleaned with acetone and leached with mild acids where surficial carbonates (caliche) were still observed. A large individual silicate inclusion (~130 mg) in Miles was isolated from the metal using aqua regia on a hot plate (80°C) for 48 h. Sample powders were dissolved in high pressure Teflon vessels (Parr bombs) following methods described in Bouvier et al. (2008).

An aliquot of about 1-5% was used for trace element analysis, a 10 % aliquot for isotope dilution, and the remainder was used for unspiked Nd and Sm isotopic analyses (see section 2 of the Supplementary Information).

Two methods of REE separation were used for unspiked samples of this study: (1) cation exchange separation with 2-methylactic acid (2MLA) for Itqiy, Tirhert (1), NWA 7034 and Khor Temiki (see Bouvier and Boyet, 2016 for details); and (2) Ln-Spec-based method for the other samples. This last method is fully described by Garçon et al. (2018) and uses $NaBrO_3$ to oxidise and remove Ce. Samples were processed twice on that column and a final purification step of Nd is made on a fine-grained 20-50 μm Ln-Spec resin. Samarium was separated from the other REE using 2 mL Biorad Polyprep® columns filled with the cation resin AG 50W-X8 in 2-methylactic acid medium.

2.3   Nd isotopic compositions

Thermo Scientific[TM] Triton and Triton Plus thermal ionisation mass spectrometer (TIMS) were used at LMV for the Nd and Sm isotopic analyses of unspiked samples.

For Nd, samples from 150 ng to 1000 ng were loaded in 2 M HCl on outgassed zone-refined Re filament using H_3PO_4. The analysis was made in different modes according to the amount of Nd available. Standard isotopic measurements for each method are given in Table S2 and data with analytical methods used for each sample are reported in Table 1. All Nd compositions were normalised to $^{146}Nd/^{144}Nd = 0.7219$ using an exponential law to correct mass fractionation.

Samples with low Nd content (< 200 ng) were run in static mode on Faraday cup detectors which were less than 6 months old. Other samples were analysed dynamically using either the 2-lines dynamic method described in Bouvier and Boyet (2016) or the 4-lines dynamic method developed by Garçon et al. (2018) when a larger mass of Nd was available, typically above ~ 250 ng.

The 4-line dynamic method developed by Garçon et al. (2018) provides better precision on Nd stable isotope ratios and long-term reproducibility. This method requires large amounts of samples, typically 500-700 ng Nd, but a reasonable precision can be achieved with 250 ng Nd as demonstrated here with NWA 11119 and Miles samples. Intensities measured for the samples ranged from 0.6 to 8×10^{-11} A for ^{142}Nd in the samples. The ratios were calculated for each sample as an average of all dynamic ratios of every cycle.

All ratios are corrected for mass fractionation using the exponential law and $^{146}Nd/^{144}Nd = 0.7219$. Errors reported for individual measurements correspond to 2 × standard error (SE). The external reproducibility

is assessed using the JNdi-1 standard reference for each session because of the long-term drift observed in static methods of measurement (Garçon et al., 2018) and is reported as 2 × standard deviation (SD). The reproducibility ranges from 4-13 ppm for $^{142}Nd/^{144}Nd$, 2-9 ppm for $^{143}Nd/^{144}Nd$, 1-13 ppm for $^{145}Nd/^{144}Nd$, 4-15 ppm for $^{148}Nd/^{144}Nd$ and 11-34 ppm for $^{150}Nd/^{144}Nd$ for all series irrespective of the load and method used. All μ values are calculated with the standard measured in the same session with a similar load to avoid drifting related to the cup ageing, following this equation:

$$\mu \; ^iX = \left(\frac{^iX/^nX_{sample}}{^iX/^nX_{standard}} - 1 \right) \times 10^6$$

where $^iX/^nX$ stands for the isotope ratio for an element X with isotopes i and n for the normalising isotope.

3. Mass-independent stable Nd isotope composition of achondrites and planetary bodies

The Nd isotope compositions of the samples measured in this study are reported in Table 1. Several isotopic ratios are not discussed in the main text (see section 6 of the Supplementary Information): 1) $^{142}Nd/^{144}Nd$ and $^{143}Nd/^{144}Nd$ due to their radiogenic nature and 2) $^{150}Nd/^{144}Nd$ the because the current level of precision of about 20 ppm (2 SD) is too low to distinguish achondrites. Only $^{145}Nd/^{144}Nd$ and $^{148}Nd/^{144}Nd$ ratios are considered thereafter. The Nd isotope composition of the samples is presented for each group below. A summary of the Nd isotope composition of achondrites and chondrites groups as well as planetary bodies including results from the literature is reported in Tables 2, S3 and S6. Achondrites and planetary samples Nd mass-independent stable isotope compositions are compared with chondrites and CAI in Figure 1.
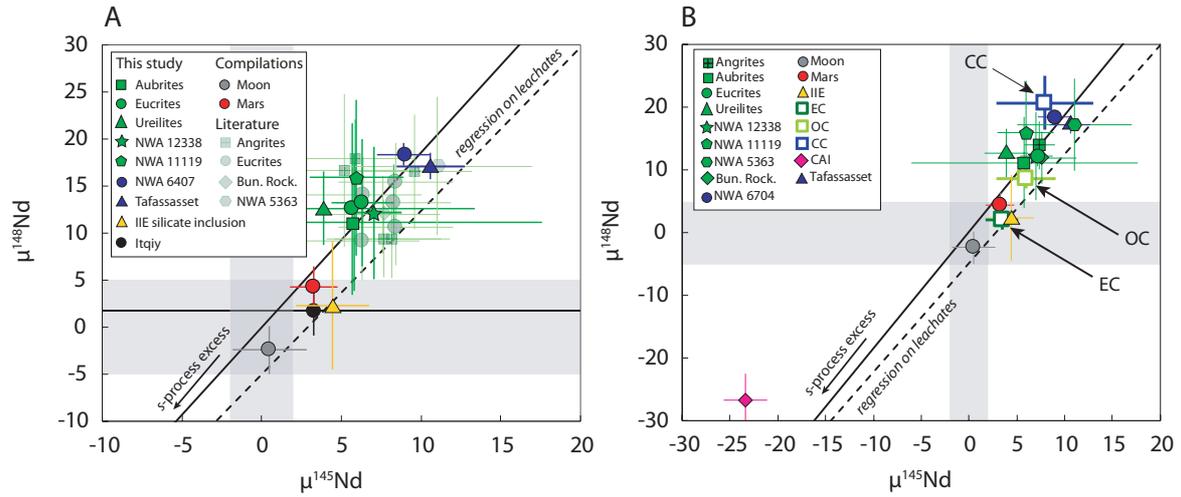
Figure 1: A) $\mu^{145}Nd$ - $\mu^{148}Nd$ compositions of NC achondrite meteorites measured in this study (green) and literature (light green) and planetary bodies. Non-carbonaceous achondrites are represented in green symbols while carbonaceous achondrites are in blue symbols. (Bun. Rock.=Bunburra Rockhole) B) $\mu^{145}Nd$ - $\mu^{148}Nd$ compositions of achondrites groups and planetary bodies compared with mean chondrite groups (EC=enstatite, OC=ordinary and CC=carbonaceous) compositions and CAI. Data sources are available in the Supplementary Information and Table S3, S4, S5 and S6. The grey areas represent the external uncertainty of JNdi-1 standards using the 4 lines-dynamic method (Table S2). The *s*-process composition is from Bisterzo et al. (2014). The leachates regression is calculated using data from Qin et al. (2011a) and Boyet and Gannoun (2013). See text for more details.

3.1   Eucrites

Eucrite samples analysed in this study consist of Tirhert and NWA 11001. In addition, five eucrites analysed by Render and Brennecka (2021) are included in the eucrite mean composition. Data from Boyet and Carlson (2005), the only other study that reports stable Nd isotope composition for eucrites, is not included here because precision on stable isotopes is significantly lower than our current dataset. Incorporating that data gives a very similar average value but with larger errors. Average compositions of Tirhert and NWA 11001 are determined from the individual measurements reported in this study. The mean Nd isotope composition of eucrite is calculated from the seven meteorites reported so far and yield a $\mu^{145}Nd = 7.1 \pm 0.9$ and $\mu^{148}Nd = 12.6 \pm 1.6$ (2 standard errors, SE, n=7).

3.2   Ungrouped achondrites

Four ungrouped meteorites from the NC (NWA 11119, NWA 12338) and C (NWA 6704, Tafassasset) groups were analysed for this study. All achondrites display well-resolved $\mu^{145}Nd$ and $\mu^{148}Nd$ anomalies. Ungrouped achondrites are considered individually as they sample different parent bodies. NWA 12338 has the lowest $\mu^{145}Nd$ and $\mu^{148}Nd$, which agree very well with those of eucrites and Bunburra Rockhole

reported by Render and Brennecka (2021). Carbonaceous achondrites along with NWA 11119 have the most positive μ^{148}Nd, similar to the value of NC NWA 5363 ungrouped achondrite (paired with NWA 5400) reported by Burkhardt et al. (2016).

3.3 Enstatite achondrite, ureilite, iron silicate inclusion, and angrite meteorites

The enstatite achondrites denomination covers aubrites and ungrouped achondrites chiefly composed of enstatite. Khor Temiki aubrite (μ^{145}Nd = 5.8 ± 7.3 and μ^{148}Nd = 11.0 ± 11.8, 2 SD) and Itqiy (average: μ^{145}Nd = 3.2 ± 16.8; μ^{148}Nd = 1.8 ± 16.7, 2 SD) Nd isotope compositions are measured with larger errors due to much lower Nd content in these samples but are undistinguishable from the terrestrial standard composition.

Catalina 037 is a pigeonite and augite-bearing ureilite. It had just enough Nd (in over 3 g dissolved) to be analysed in static mode yielding μ^{145}Nd = 3.9 ± 2.2 and μ^{148}Nd = 12.6 ± 3.9 (2 SD).

Miles is a IIE non-magmatic iron meteorite with silicate inclusions composed of plagioclase, augite and orthopyroxene. The individual silicate inclusion analysed in this study has a composition indistinguishable within errors from the standard with μ^{145}Nd = 4.4 ± 2.3 and μ^{148}Nd = 2.3 ± 6.8 (2 SD). Neodymium isotope compositions of angrites have been reported by Saji et al. (2020) and Render and Brennecka (2021). The average composition of angrites, excluding NWA 4801 (see Render and Brennecka, 2021), is μ^{145}Nd = 7.3 ± 1.6 and μ^{148}Nd = 13.9 ± 3.8 (2 SE, n=5).

3.4 Martian meteorites and the Moon

The martian polymict breccia NWA 7034 (n=3) was analysed with a 2-line dynamic method in this study and yields a composition indistinguishable from the standard within errors for μ^{145}Nd and μ^{148}Nd. Several literature studies have reported Nd isotope compositions for martian meteorites with various levels of precision as most studies focused on ^{142}Nd (Table S4). The weighted mean composition of Mars obtained is μ^{145}Nd = 3.3 ± 1.5 and μ^{148}Nd = 4.3 ± 2.1 (2 SE, n = 51 and 39 respectively).

Lunar samples were not analysed in this study but literature data is relatively abundant (Table S5). As lunar samples are more commonly affected by neutron capture effects, only samples with ε^{149}Sm < 6 were included in this compilation and all corresponding Nd compositions were corrected for neutron

capture effects. We find a weighted mean composition for the Moon of μ^{145}Nd = 0.4 ± 2.3 and μ^{148}Nd

= -1.3 ± 2.5 (2 SE, n = 42).

	Classification	Serie	Method	Nd (ppm)	Sm (ppm)	$^{147}Sm/^{144}Nd$	I ^{142}Nd (V)	$\mu^{142}Nd$	±	$\mu^{142}Nd_B$	$\mu^{143}Nd$	±	$\mu^{145}Nd$	±	$\mu^{148}Nd$	±	$\mu^{150}Nd$	±	$^{146}Nd/^{144}Nd$	$^{142}Ce/^{142}Nd$ ppm	$^{144}Sm/^{144}Nd$ ppm	cycles
Ungrouped achondrites																						
NWA 6704	Achon-ung	4	Dyn 4L	0.30	0.10	0.1995	4.45	-12.0	1.9	-24.1	1515	1	8.9	1.7	18.3	1.2	34.4	8.6	0.7218	0.3	0.1	540
Tafassasset	Achon-ung	4	Dyn 4L	0.28	0.09	0.2027	3.39	-28.0	2.4	-33.2	1241	1	10.6	2.1	17.1	1.4	12.8	11.9	0.7223	0.1	0.1	420
NWA 11119 WR	Achon-ung	3	Dyn 4L	1.19	0.51	0.2606	0.6	90.1	4.7	-5.8	4848	3	6.0	2.9	15.9	8.3	32.3	22.5	0.7211	304.5	0.0	220
NWA 11119 MS1	Achon-ung	3	Dyn 4L	1.51	0.64	0.2577	0.8	78.0	2.0	-15.4	4751	1	7.9	1.3	12.7	3.7	25.1	9.5	0.7220	0.0	0.0	250
NWA 11119 ave.										**-10.6**			**6.9**	**2.8**	**14.3**	**4.5**	**28.7**	**10.2**				
NWA 12338 (1)a	Achon-ung	4	Dyn 4L	2.23	0.73	0.1972	5.57	-9.0	1.1	-9.4	1050	1	7.7	1.0	9.6	0.8	16.2	5.6	0.7219	1.2	9.3	1080
NWA 12338 (1)b	Achon-ung	4	Dyn 4L	2.23	0.73	0.1972	5.89	-9.6	1.7	-10.0	1051	1	6.4	1.5	14.6	1.2	23.6	7.7	0.7238	0.0	0.0	510
NWA 12338 ave.										**-9.7**			**7.0**	**1.7**	**12.1**	**7.0**	**19.9**	**10.3**				
Eucrites																						
Tirhert (1)	Eucrite	2	Dyn 2L	2.77	0.91	0.1984	1.3	-19.8	3.9	-13.1	720	1	3.0	3.6	15.8	6.0	18.4	10.8	0.7222	27.9	0.1	440
Tirhert (2)	Eucrite	4	Dyn 4L	-	-	-	5.14	-11.0	1.3	-11.8	1123	4	8.4	1.2	9.3	0.8	8.2	5.7	0.7206	0.1	0.1	1080
Tirhert ave.									1.9	**-12.5**			**5.7**	**7.7**	**12.5**	**9.1**	**13.3**	**14.4**				
NWA 11001 (1)a	Eucrite	4	Dyn 4L	2.64	1.01	0.2313	7.5	42.4	1.4	-10.5	3120	1	7.3	1.3	13.7	0.9	25.5	6.4	0.7214	0.0	0.0	540
NWA 11001 (1)b	Eucrite	4	Dyn 4L	2.64	1.01	0.2313	7.38	46.2	1.3	-6.8	3122	1	5.2	1.3	12.8	0.9	33.0	6.4	0.7235	0.0	0.0	540
NWA 11001 (2)	Eucrite	4	Dyn 4L	2.67	1.08	0.2452	4.86	59.4	2.1	-13.5	3904	1	7.0	1.8	9.1	1.3	13.9	9.1	0.7219	0.1	0.2	540
NWA 11001 (3)	Eucrite	4	Dyn 4L	-	-	-	2.84	73.5	2.4	-26.4	4968	1	5.9	2.1	17.3	1.5	16.7	11.7	0.7211	0.7	0.2	540
NWA 11001 ave.									17.1	**-14.3**			**6.3**	**2.0**	**13.2**	**6.8**	**22.3**	**17.4**				
Mars																						
NWA 7034 (1)	Martian polymict breccia	1	Stat	20.30	5.61	0.1668		-41.9	5.9	3.9	-717	6	-1.3	5.2	0.2	0.0	0.2	0.0		21.8	12.3	
NWA 7034 (2)		2	Dyn 2L	20.30	5.61	0.1668	2.3	-43.6	5.2	2.3	-724	5	-3.3	4.8	3.4	7.8	-12.4	9.7	0.7233	3141.7	0.1	240
NWA7034 R		2	Dyn 2L	8.96	2.74	0.1852	1.3	-35.9	4.9	-34.2	973	5	-0.2	4.4	10.5	7.5	-3.4	10.5	0.7227	2404.8	0.2	300
Enstatite achondrites																						
Khor Temiki	Aubrite	2	Dyn 2L	0.43	0.16	0.2206	1.0	17.6	8.6	-19.1	2549	8	7.1	7.3	11.3	11.8	54.7	18.5	0.7235	164.8	0.0	200
Itqiy (1)	EH7	2	Dyn 2L	0.07	0.06	0.5010	0.6	312.5	11.0	-21.2	14285	10	-2.7	9.0	2.8	16.7	34.3	23.7	0.7235	113.1	0.3	180
Itqiy (2)	EH7	2	Stat	0.09	0.07	0.4438	0.7	435.9	11.0	-11.7	18807	10	9.2	8.0	0.8	15.7	-18.8	20.5	0.7223	235.3	0.2	200
Itqiy ave.										**-16.5**			**3.2**	**16.8**	**1.8**	**2.8**	**7.7**	**75.0**				
Catalina 037	Ureilite	4	Stat	0.06	0.02	0.2468	7.5	72.9	3.0	-12.1	4412	2	3.9	2.2	12.6	3.9	29.9	5.3	0.7226	0.6	0.1	820
Miles (sil. inclusion)	IIE	3	Dyn 4L	1.71	0.71	-	2.4	52.6	4.9	-22.7	4028	4	4.4	2.3	2.3	6.8	13.1	17.0	0.7220	84.6	198.7	250
Rock standards																						
BCR-2	Earth	2	Dyn 2L	28.19	6.45	0.1383	1.7	3.7	3.2		1014	3	-2.6	2.9	9.1	5.0	11.9	7.0	0.7227	128.3	0.2	440
BCR-2	Earth	3	Dyn 4L				5.5	2.3	3.6		1019	5	-0.5	2.5	-4.0	5.6	-14.4	9.4	0.7213	0.0	0.0	540
BHVO-2	Earth	3	Dyn 4L				4.2	5.9	3.6		1706	5	1.5	2.5	4.7	5.6	10.9	9.4	0.7216	0.1	0.0	540
Average								4.0	3.6				-0.5	4.2	3.3	13.3	2.8	29.7				

5

6

Table 2: Nd isotope composition of achondrite and chondrite groups as well the Moon and Mars. References can be found in the section 7 of the Supplementary Information. Errors are 2 SE or 2 SD for n<4 and are reported in ppm.

Meteorite group	$\mu^{142}Nd_B$	±	$\mu^{145}Nd$	±	$\mu^{148}Nd$	±	n
Ung. CC achondrites							
NWA 6704	-24.1	1.9	8.9	1.7	18.3	1.2	1
Tafassasset	-33.2	2.4	10.6	2.1	17.1	1.4	1
NC achondrites							
NWA 11119	-10.6	13.7	6.9	6.0	14.3	7.3	1
NWA 12338	-9.7	0.9	7.0	2.9	12.1	8.3	1
Bunburra Rockhole	-6.3	4.4	7.6	3.6	11.9	5.7	1
NWA 5363	-16.0	5.9	11.0	6.0	17.1	7.3	1
Angrites	-13.8	3.2	7.3	1.6	13.9	3.8	5
Ureilites	-12.1	3.0	3.9	2.2	12.6	3.9	1
Eucrites	-14.8	2.3	7.1	0.9	12.6	1.6	7
Aubrites	-19.1	8.6	7.1	7.3	11.3	11.8	1
IIE (silicate inclusion)	-22.7	4.9	4.4	2.3	2.3	6.8	1
Mars			3.3	1.5	4.3	2.1	51/32[a]
Moon			0.4	2.3	-1.3	2.5	42
Enstatite chondrites	-11.4	2.7	3.3	1.7	2.2	1.4	21
Ordinary chondrites	-13.0	3.0	2.7	3.1	8.1	1.6	14
Carbonaceous chondrites[b]	-28.9	6.1	8.0	5.1	20.3	4.3	7
CAI	-7.5	3.3	-23.4	2.3	-26.8	4.3	15

[a]Not all publications on martian meteorites report all isotope ratios. We included 51 measurements for $\mu^{145}Nd$ and 32 for $\mu^{148}Nd$.

[b]The mean composition of carbonaceous chondrites used here does not include the highly variable CV chondrites because of the varying content in CAI that greatly affects their Nd isotope composition as well as CI chondrites and Tagish Lake that have a distinct composition from other CC groups.

4. Discussion

4.1 Gap in the Nd isotope composition between NC achondrites and chondrites

The C-NC isotope dichotomy divides both chondrites and achondrites into two distinct groups that coexisted separately in the protoplanetary disc (Trinquier et al., 2007; Leya et al., 2008). Compared to other heavy elements such as Mo, Nd isotope ratios normalised to $^{146}Nd/^{144}Nd$ lack resolution on *p*- and *r*- nucleosynthetic processes to identify this dichotomy which consists primarily in an excess of *r*-process and depletion in *p*-process or variable *s*-process compositions (Stephan et al., 2019; Bouvier and Boyet, 2016; Kruijer et al., 2020). Indeed, excess or depletion in *r*-process coincides with the *s*-process mixing line and large anomalies in the *p*-process are only identified with $\mu^{142}Nd$.

The mass-independent Nd isotope composition of achondrites and planetary bodies (Earth, Mars, and Moon) distinguishes two groups that reveal a new dichotomy related to the time of accretion. On the

one hand, differentiated NC and C achondrites originating from early-formed planetesimals display

significant anomalies from the terrestrial JNdi-1 standard on the ^{148}Nd/^{144}Nd ratio with + 12 to +18 ppm

excesses. On the other hand, planetary samples originating from the Moon and Mars have Nd isotope

compositions indistinguishable from the terrestrial composition. A silicate inclusion from Miles (IIE

iron) appears as an outlier among planetesimal achondrites as it displays composition similar to

planetary samples. The two carbonaceous achondrites (NWA 6704 and Tafassasset) studied are related

to CR chondrites (Gardner-Vandy et al., 2012; Sanborn et al., 2019) and all share the same Nd isotope

composition. Interpretation of the CC achondrites composition relative to CC chondrites therefore

requires additional measurements of such meteorites.

NC achondrites display stronger anomalies in comparison to their chondritic counterparts (ordinary and

enstatite chondrites). These achondrites are intermediate in composition between ordinary and

carbonaceous chondrites. This observation is corroborated by a recent study on eucrites and angrites

(Render and Brennecka, 2021). The difference between NC achondrites and chondrites is also observed

for other elements such as Zr, Mo and Cr (Figure 2). The distinction between achondrites and ordinary

chondrites is not clear with ε^{96}Zr when including compositions from different studies, but Render and

Brennecka (2021) suggest that ordinary chondrites display resolved anomalies from angrites. However,

concerning Mo and Cr, achondrites are clearly resolved from ordinary and enstatite chondrites.

Chromium isotope composition reflects many nucleosynthetic processes and the anomalies cannot be

strictly compared to those of heavy elements. The Nd and Cr isotope compositions of achondrites are

not well correlated (Figure 2). In fact, the spread in ε^{54}Cr of planetesimal achondrites is not observed in

μ^{148}Nd, which is rather homogeneous. Nd and Cr are hosted in different carriers, SiC and oxides,

respectively, and are not produced in the same stellar environment. Chromium-54 is predominantly

produced in type Ia or II supernova (Dauphas et al., 2010; Qin et al., 2011) and Nd s-process in

asymptotic giant branch (AGB) stars (Hoppe and Ott, 1997). About 40% of Nd nuclides are produced

by r-process but are not hosted in a presolar carrier (Qin et al., 2011; Boyet and Gannoun, 2013; Bisterzo

et al., 2014). Thus, it is difficult to interpret this general trend as a true correlation.

A correlation between Nd, Zr and Mo nucleosynthetic anomalies has been suggested by Render et al.

(2017) and Render and Brennecka (2021). Even if the carriers of the anomalies for these elements are

54   different, the observed trends appear to reflect *s*-process variations. The advantage of Mo lies in its

55   moderately siderophile nature that allows for the comparison of iron meteorites with stony achondrites.

56   Most iron and stony NC achondrites display more positive Mo isotopes anomalies compared to ordinary

57   chondrites. The IAB-MG, -sLL, -SLM, IIICD and IIE irons, aubrites and some ungrouped achondrites

58   are exceptions and display lower or similar Mo anomalies than ordinary chondrites (Budde et al., 2019;

59   Hilton and Walker, 2020). The distinction between achondrites and chondrites is therefore not restricted

60   to Nd and is a significant feature that is observed particularly for heavy elements. This feature may

61   transcribe: (1) a spatial heterogeneity, or (2) a temporal variation in the protoplanetary disc, or both.

62
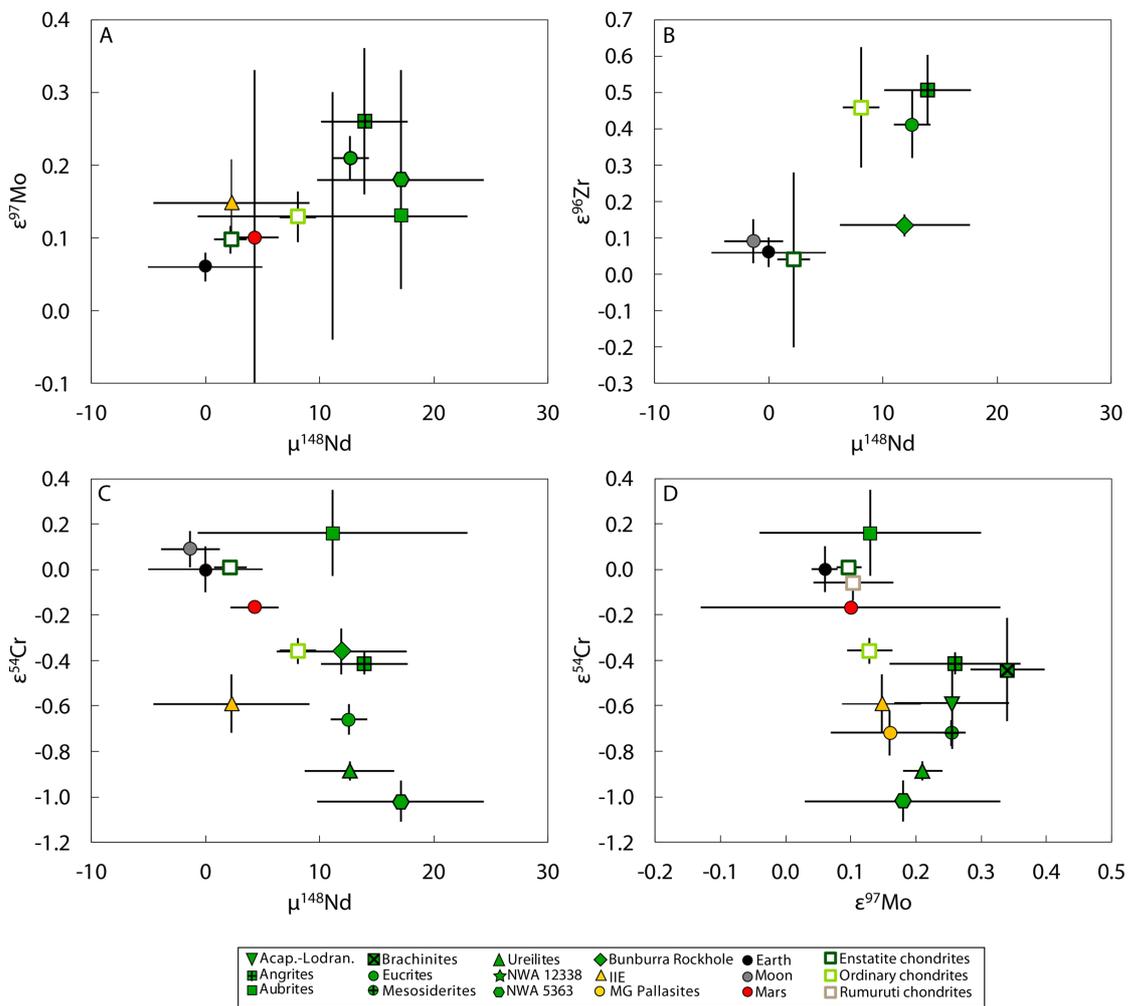
Figure 2: Non-carbonaceous achondrites and chondrites groups average compositions for μ^{148}Nd, ε^{97}Mo, ε^{96}Zr and ε^{54}Cr. Data sources for Mo, Zr and Cr isotope compositions are reported in Table S7, S8 and S9. A broad correlation is observed for all systems from an end-member represented by the Earth-Moon system to early planetesimal achondrites. Chromium isotope composition reflects different nucleosynthetic processes and the trend has another signification in μ^{148}Nd- ε^{54}Cr and ε^{97}Mo- ε^{54}Cr diagrams.

68

4.2 Variation of the Nd nucleosynthetic anomalies within the inner regions of the protoplanetary disc

4.2.1 Oxygen fugacity gradient within the protoplanetary disc as a proxy for heliocentric distance

Previous studies have proposed that the Nd isotope composition of chondrites is related to the heliocentric distance of accretion of their respective parent bodies (Bouvier and Boyet, 2016; Burkhardt et al., 2016; Render et al., 2017, Render and Brennecka, 2021). Defining the location of formation of a meteorite parent body is challenging and some authors have proposed that the volatile elements content and oxygen fugacity in meteorites could provide clues in this regard (e.g. Grossman et al., 2008; Morbidelli et al., 2012). Concerning chondrites, this distinction seems plausible as the gradient in the Nd isotope composition matches a general trend of volatile depletion and oxidation in chondrites from enstatite to carbonaceous chondrites. Enstatite chondrites are extremely reduced, possibly even more reduced than the solar nebula conditions (Grossman et al., 2008). Ordinary chondrites display a range of oxidation from H to LL subgroups and carbonaceous chondrites are generally more oxidized with barely no metal in aqueously altered groups. The distribution of asteroids in the main belt highlights the original zonation in the Solar System with the prevalence in the inner parts of the asteroid belt of E- and S-type asteroids, possible parent bodies of enstatite and ordinary chondrites respectively, whereas C-type (carbonaceous) asteroid populate the outer parts (DeMeo and Carry, 2014). Consequently, the oxygen fugacity is considered as a proxy of the heliocentric distance of accretion of the parent body of a given meteorite group.
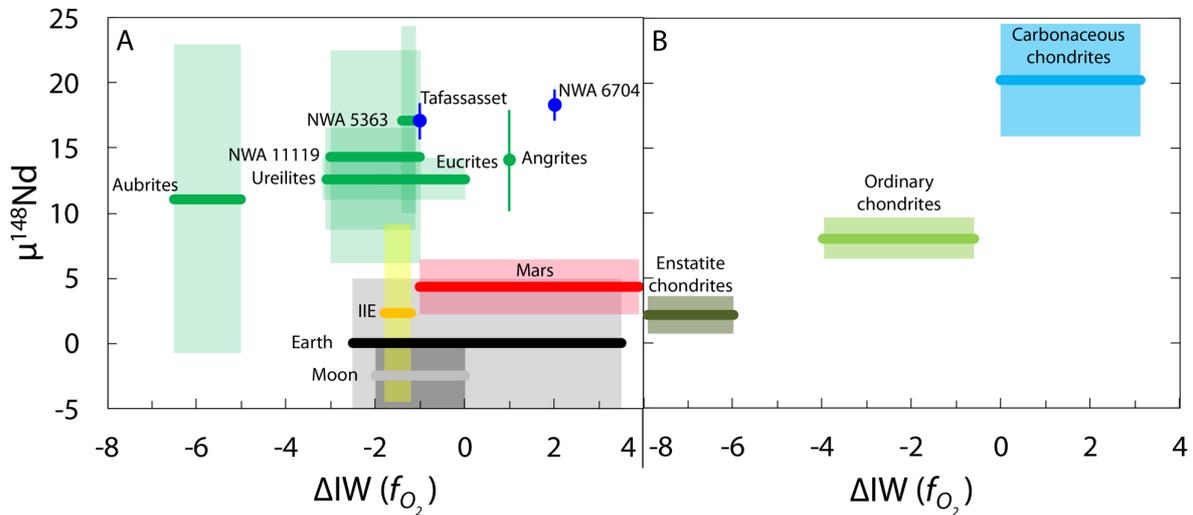
However, the heliocentric distance of achondrite parent bodies when they formed is much more difficult to assess due to the loss of volatile elements during degassing of the magma ocean and the oxygen fugacity variation during the differentiation events on planetesimals. Render and Brennecka (2021) recently suggested that the correlation between Nd and Zr nucleosynthetic anomalies and water content of chondrites implies that nucleosynthetic anomalies are a proxy for the heliocentric distance of accretion. Our dataset that includes various types of achondrites suggests otherwise. In the search for a proxy of the heliocentric distance, the oxygen fugacity could provide significant information. Despite its variation during magmatic processes, the oxygen fugacity gives a broad estimation of the nebular reservoirs of achondrites.

98   The oxidation degree, or oxygen fugacity (f_{O2}), of the meteorites can be quantified with various methods

99   including XANES (X-Ray Absorption Near Edge Structure) studies and thermodynamical calculations

100   based on the chemical composition of various phases. The oxygen fugacity is expressed relative to the

101   Iron-Wüstite buffer (ΔIW) in the following sections. Crustal rocks generally display higher f_{O2} than their

102   primary melt, as exemplified on Earth with the primitive mantle of about ΔIW -2 and andesites up to

103   ΔIW +6 (Righter et al., 2016). Therefore, the oxygen fugacity of achondrites reported here corresponds

104   to the higher end of the f_{O2} conditions of their respective parent bodies.

105   The distribution of Nd nucleosynthetic anomalies relative to f_{O2} differs when considering achondrites

106   and chondrites (Figure 3). The μ^{148}Nd of chondrite groups increase with heliocentric distance, whereas

107   the planetesimal-derived achondrites, excluding Miles, display a similar μ^{148}Nd while spanning over a

108   large range of f_{O2} (-6.5 < ΔIW < 1). Mars, the Earth and the Moon formed in f_{O2} conditions similar to

109   that of achondrites but display much lower μ^{148}Nd anomalies. This observation conflicts with the

110   interpretation of a heliocentric distribution of the nucleosynthetic anomalies of many elements in

111   achondrites and chondrites alike. In addition, the comparison of Nd and Mo nucleosynthetic anomalies

112   of parent bodies with their formation locations within the solar system inferred by the model of Desch

113   et al. (2018) yields a similar interpretation (Figure 4).

114   Spatial distribution has also been invoked to explain the distribution of the nucleosynthetic anomalies

115   in meteorites (e.g. Burkhardt et al., 2016; Fischer-Gödde and Kleine, 2017; Render et al., 2017; Ek et

116   al., 2020; Render and Brennecka, 2021). This interpretation is based on three types of chondrites

117   (enstatite, ordinary and carbonaceous) and the correlation between nucleosynthetic anomalies and H_2O

118   content, the latter inferred to increase with heliocentric distance due to the thermal gradient in the

119   protoplanetary disc. Most chondrites formed coevally and their heterogeneous nucleosynthetic

120   composition needs to be spatially-distributed. When Rumuruti chondrites are considered, this

121   relationship breaks down for Cr and Mo for instance. Indeed, these chondrites are relatively oxidised

122   and contain more water than other non-carbonaceous chondrites (Krot et al., 2014), whereas their

123   nucleosynthetic composition is close to enstatite chondrites for Cr (Figure 2). Nucleosynthetic

124   anomalies for Mo are variable and are either lower or higher in magnitude than ordinary chondrites

125   considering Budde et al. (2019) or Yokoyama et al. (2019) data, respectively. As demonstrated above,

126 achondrite nucleosynthetic anomalies are not distributed following the heliocentric distance (Figures 3

127 and 4).

128

129

Figure 3: μ^{148}Nd (in ppm) shown against a proxy of the heliocentric distance using the redox conditions expressed relative to the IW (Fe-FeO) equilibrium, in (A) achondrites and (B) chondrites. The sources for achondrites and chondrites data are the same as those in Figure 1. Oxygen fugacities are all from Righter et al. (2016), except for ungrouped achondrites that are from Srinivasan et al. (2018) for NWA 11119, Burkhardt et al. (2017) for NWA 5363, Gardner-Vandy et al. (2012) for Tafassasset and Hibiya et al. (2019) for NWA 6704.

136

137 4.2.2   Temporal distribution of the Nd nucleosynthetic anomalies

138 Increasingly precise Hf-W and Al-Mg short-lived radiometric ages show that accretion ages of iron

139 meteorites are older than chondrules, which start to form around 2 Ma after CAI based on Al-Mg

140 systematics (e.g. Kruijer et al., 2017; Pape et al., 2019). Older ages of chondrules obtained by Pb-Pb

141 (Bollard et al., 2017) or Mn-Cr chronometry (Zhu et al., 2019) may be caused by several processes. For

142 instance, precursor compositions not fully resetting during chondrule melting events, as suggested by

143 the abundance of volatile elements in chondrules (Mahan et al., 2018); and Th/U ratio variability in

144 chondrules (Blichert-Toft et al., 2020) may result in erroneous ages. The Al-Mg systematics are not

145 exempt from debate, as the homogeneity of the initial abundance of ^{26}Al is still contested but involve

146 refractory elements and agree with the Hf-W system chronology (Nagashima et al., 2018).

147 The accretion ages of differentiated achondrites are more difficult to constrain owing to thermal and

148 geochemical models. Sugiura and Fujiya (2014) suggested that most achondrite parent bodies accreted

149 before chondrules and have similar or younger accretion ages to that of iron meteorite parent bodies.

150 NWA 5363/5400 formed around 2.2 ± 0.8 Ma after CAI based on I-Xe age and Hf-W modelling

151 (Burkhardt et al., 2017) and NWA 11119 accretion age has not been reported in the literature. However,

152 the rock crystallised at 4564.8 ± 0.3 Ma, thus within 2-3 Ma of CAIs according to Al-Mg dating

153 (Srinivasan et al., 2018), and therefore its parent body must have accreted in the period deduced for

154 other basaltic achondrites (e.g., angrites, eucrites, ureilites, ungrouped such as NWA 6704 or

155 Tafassasset). Thus, the parent bodies of achondrites accreted before chondrules even formed or were at

156 least preserved and accreted to form the chondrites.

157 In contrast, planetary bodies accreted over a longer period of time, spanning several millions of years

158 after chondrule formation. Some achondrites also formed later, notably the IAB and IIE parent bodies

159 according to the Hf-W systematics. The Hf-W ages of the IAB and IIE irons are possibly reset due to

160 impact melting and re-equilibration, nevertheless, the oldest model ages agree with a rather late

161 accretion around 1.5 Ma, thus significantly later than other iron groups (Hunt et al., 2018; Hilton and

162 Walker, 2020; Kruijer and Kleine, 2019). Despite the rather unprecise accretion ages, Nd and Mo

163 nucleosynthetic anomalies in achondrites and chondrites of the non-carbonaceous group appear to

164 roughly decrease with the age of accretion of the parent bodies, particularly around 1.5 Ma (Figure 4).

165 This trend is not observed in carbonaceous achondrites that are thought to originate from CR-related

166 reservoirs (Gardner-Vandy et al., 2012; Sanborn et al., 2019) and display the same Nd isotope

167 composition with CR chondrites. Three groups can be distinguished in non-carbonaceous meteorites

168 based on chronological constraints: 1) early planetesimal achondrites; 2) chondrites; 3) late planetesimal

169 achondrites and planetary bodies.

170 Several studies have suggested a temporal distribution of the nucleosynthetic anomalies (e.g. Sugiura

171 and Fujiya, 2014 and Schiller et al., 2018). Using the Cr isotope systematics, Sugiura and Fujiya (2014)

172 evidenced a correlation between time of accretion and $\varepsilon^{54}Cr$ anomalies. Hilton and Walker (2020) also

173 identified a correlation between $\mu^{182}W$ and $\mu^{97}Mo$ indicating a possible temporal evolution of the Mo

174 nucleosynthetic anomalies of non-carbonaceous iron meteorites. Our Nd data corroborate these findings

175 and highlight the gap between the nucleosynthetic signatures of achondrites, chondrites, and planetary

176 bodies.

177   We argue that the temporal distribution of Nd and Mo nucleosynthetic anomalies are likely, but

178   nevertheless do not rule out a spatial heterogeneity of the anomalies. The range of nucleosynthetic

179   anomalies observed in early planetesimal achondrites cannot be related to a temporal evolution and may

180   reflect spatial heterogeneities in different parts of the inner solar system in which radial mixing is

181   significant as exemplified in accretion models (e.g. Raymond and Morbidelli, 2020). Nonetheless, the

182   large change in Nd and Mo nucleosynthetic composition between early planetesimals and planetary

183   bodies appears temporally related and occurred relatively late. This is also demonstrated with the lower

184   intensity of the anomalies of the two late-formed iron meteorite groups: the IIE that display comparable

185   Nd and Mo nucleosynthetic anomalies with OC, and the IAB that are undistinguishable from Earth's

186   Mo composition (Figure 4).
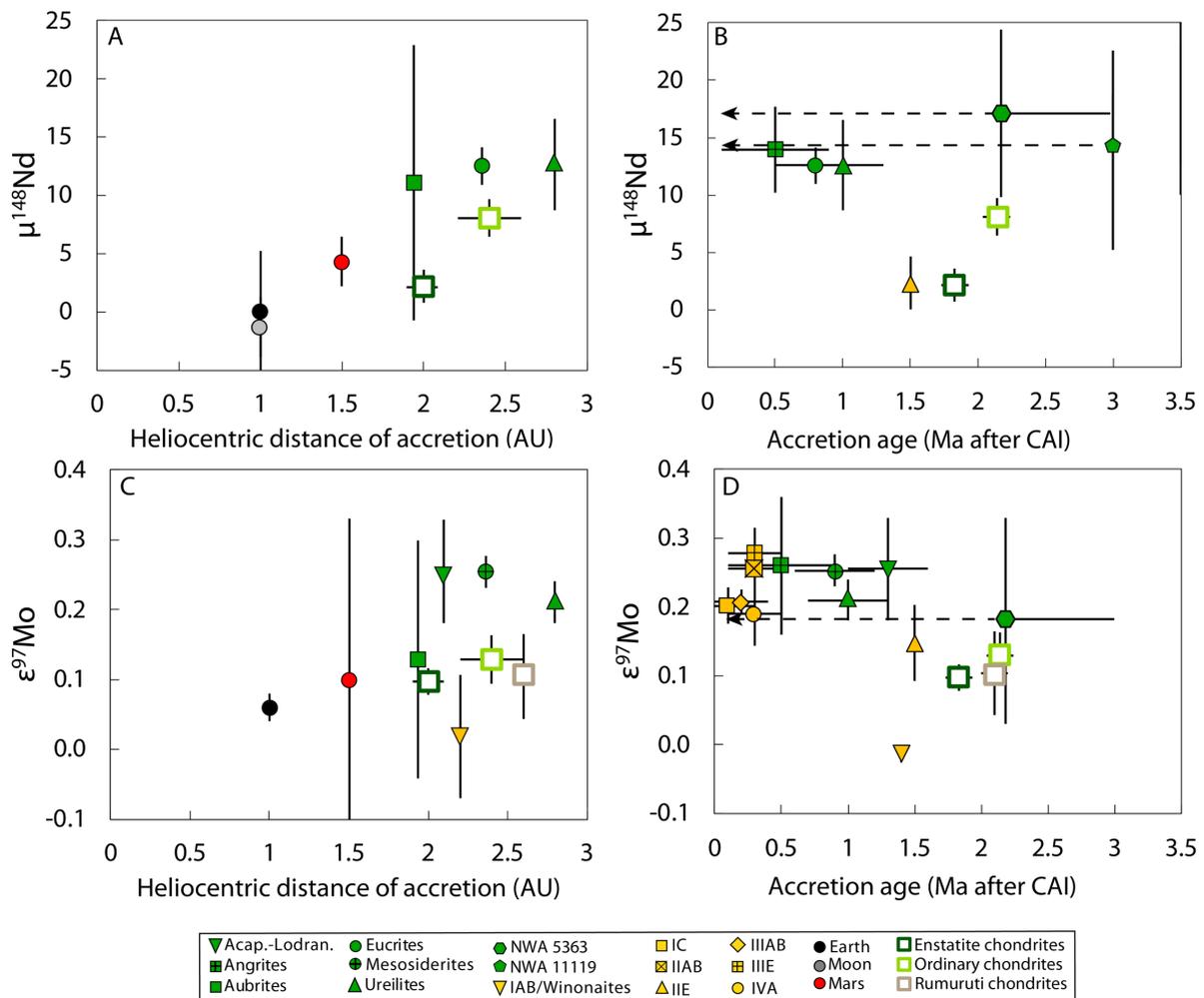
187

188 Figure 4: Distribution of μ^{148}Nd (A) and ε^{97}Mo (C) with the putative heliocentric distance of accretion
189 estimated by Desch et al. (2018) and actual position of planetary bodies, and with the estimated age of
190 accretion determined by Sugiura and Fujiya (2014) for achondrites and chondrites, Spitzer et al. (2020)

191 (Table S8) and references therein for iron meteorites. All meteorite groups are not plotted for all graphs,
192 as heliocentric distances and ages of accretion are not estimated for all. The age of accretion reported
193 for NWA 5363 represents a maximum, whereas the age of crystallisation is reported for NWA 11119,
194 both are likely older (Burkhardt et al., 2017; Srinivasan et al., 2018). Sugiura and Fujiya (2014) report
195 an age of 1.8 ± 0.1 Ma based on thermal evolution models for EL6 chondrites, but there is no precise
196 age for enstatite chondrite accretion or chondrule formation.

197 4.3   Thermal processing event coinciding with chondrule formation

198 4.3.1   Processes to produce heterogeneous isotopic reservoirs

199 The variation observed in Nd and Mo isotope compositions from achondrites to chondrites and later

200 formed planetary bodies can be explained by two main processes: (1) addition of compositionally

201 different matter, and (2) thermal processing. For instance, both processes have been invoked to explain

202 the NC-CC dichotomy (e.g., Trinquier et al., 2009; Nanne et al., 2019). In the light of the new Nd stable

203 isotopic data acquired on achondrites, we propose a new model. This model may also apply to other

204 elements for which the carriers of the anomalies are similar such as Zr and Ba, or different such as Mo.

205 Following the collapse of the solar nebula, the protoplanetary disc accreted progressively and grew by

206 viscous spreading. While expanding, the protoplanetary disc was continuously fed by the infalling

207 nebular cloud (Boss and Goswami, 2006). Timescales of infall depend on the initial temperature of the

208 molecular cloud and are generally short, around 100-500 ka (Yang and Ciesla, 2012). Infall of material

209 into the protoplanetary disc is therefore unlikely to have produced the difference between the Nd isotope

210 compositions of achondrites and chondrites which appeared relatively late, 1.5 Ma after CAIs. Infall of

211 anomalous material creating the variation in nucleosynthetic anomalies in meteorites is principally

212 proposed for light elements such as Cr and Ni for which the anomalies originate from supernovæ

213 products (e.g. Dauphas et al., 2010; Qin et al., 2011b; Nanne et al., 2019). Altogether, the infall scenario

214 does not explain the anomalies in heavier elements produced by *s-*, *r-* and *p*-processes (e.g. Akram et

215 al., 2015; Worsham et al., 2019; Yokoyama et al., 2019; Ek et al., 2020).

216 Astronomical observations and astrophysical models show that protoplanetary discs are thermally zoned

217 from the inside out and cool in a few million years (Boss, 1998). Thermal processing of material in the

218 protoplanetary disc is likely to have occurred in the hot and early inner solar system. Several lines of

219 evidence support the importance of thermal processing to produce variable nucleosynthetic anomalies

220 in meteorites in particular for heavy elements regarding the refractory nature of anomaly carriers (e.g.

221 Worsham et al., 2019; Ek et al., 2020).

222 ### 4.3.2 Thermal processing as the main process to produce the temporal dichotomy

223 Thermal processing involves a selective destruction of phases in a reservoir containing compositionally

224 different materials. Leaching experiments evidenced that anomalous Nd is solely hosted in presolar SiC,

225 similarly to other elements such as Ba (Boyet and Gannoun, 2013; Qin et al., 2011) and highlighted the

226 absence of pure *r*- and *p*-process Nd anomaly carriers observed in chondrites. It is very unlikely that

227 such carriers were partially destroyed during thermal processing in the protoplanetary disc. Heavy

228 elements anomalies measured in NC meteorites correspond to a binary mixing between *s*-process

229 (sometimes multiple) refractory carriers and another component devoid of extremely anomalous

230 material. The latter is considered to be composed of dust in the protoplanetary disc and representative

231 of the original composition of the protoplanetary disc material excluding *s*-process carriers, hereafter

232 referred to as "solar reservoir," equivalent to the ISM dust defined by Ek et al. (2020). The temporal

233 variation of Nd isotope compositions between achondrites and planetary materials suggests that the solar

234 reservoir material that was destroyed was somewhat homogeneous in composition. In general,

235 anomalous isotope compositions are hosted in minute grains of refractory nature, carbides, refractory

236 metals, and oxides as evidenced by leaching experiments and presolar grains studies (e.g. Zinner, 2014).

237 Because presolar grains are mostly refractory (Zinner, 2014), thermal processing is more prone to affect

238 the solar reservoir dust rather than highly anomalous presolar grains. The nature of dust in the

239 protoplanetary disc is diverse. However, matrix mineralogy in primitive chondrites as well as

240 astronomical observations of the interstellar medium and protoplanetary discs reveal the predominance

241 of amorphous silicates that would be easily altered during thermal processing (Le Guillou et al., 2015;

242 Scott and Krot, 2005; Tielens et al., 2005).

243 As bulk meteorite composition is influenced by a binary mixing, one can estimate the solar reservoir

244 composition with a mass balance using CI chondrites, considering that they contain an unaltered presolar

245 SiC content (Huss, 1997). Depending on the SiC content and Nd concentrations in SiC, the solar

246 reservoir μ^{148}Nd ranges from +113 to +2171 ppm (see section 8 of the Supplementary Information).

247   Then, considering two stages in the protoplanetary disc evolution, the early achondrite and terrestrial

248   planet formation stages, the same binary mixing can be formulated. Considering that SiC grains are not

249   affected by this thermal processing event, the only variable is the amount of presolar SiC in the two

250   stages as the destruction of solar reservoir material results in an increase of the SiC content in the bulk

251   material (Yokoyama et al., 2019; Ek et al., 2020). The mass of Nd of the solar reservoir lost between

252   the two stages to account for the composition of achondrites and planetary bodies is derived from the

253   SiC content calculated from the two mixing stages. Because SiC are particularly rich in Ba, we apply

254   the same mixing equations to μ^{135}Ba in order to compare with μ^{148}Nd. The achondrite Ba composition

255   obtained from Juvinas eucrite (Andreasen and Sharma, 2007) is not resolved from the terrestrial standard

256   (μ^{135}Ba = 5 ± 4). Nevertheless, calculations were carried out to see if the results were consistent or

257   totally nonsensical owing to the high Ba concentrations in SiC. The results using μ^{148}Nd and μ^{135}Ba in

258   function of the concentration of SiC are reported in Figure 5 and are very similar. Neodymium and Ba

259   content in SiC significantly influence the lost fraction of the solar reservoir. According to the presolar

260   SiC contents in Orgueil reported by Huss and Lewis (1995), and considering Nd and Ba contents in SiC

261   of 10 ppm to 39 ppm and 50 ppm to 400 ppm respectively, the fraction of the solar reservoir lost with

262   thermal processing ranges from 0.2 to 2.3 % to account for the difference between achondrites and

263   Earth's Nd and Ba isotope compositions. Ek et al. (2020) proposed an estimated 0.37 % of the fraction

264   of the ISM dust destroyed, based on the 0.02% *s*-process enrichment of the Earth relative to

265   carbonaceous chondrites. Our approach is different than Ek et al. (2020) as we consider only the inner

266   solar system materials. Nevertheless, the two interpretations are not mutually exclusive. The difference

267   between inner (NC) and outer (C) meteorites may reflect thermal processing in the early phases of the

268   solar system evolution. Different dynamical scenarios have been proposed to explain the separation of

269   planetary formation reservoirs with different compositions (e.g. Kruijer et al., 2017; Yokoyama et al.,

270   2019; Ek et al., 2020).

271   The effect of thermal processing on Mo isotope compositions is more difficult to constrain as *s*-process

272   Mo is hosted in various presolar grains in addition to SiC, for which the abundance is not known.

273   Interestingly, in contrast to the relative homogeneity of Nd isotope compositions, the early planetesimals

274   display variable Mo isotope compositions (e.g. Yokoyama et al., 2019; Spitzer et al., 2020). This

275 heterogeneity can be interpreted as sampling a temporally and spatially heterogeneous early

276 protoplanetary disc. Yokoyama et al. (2019) suggest that the mixing trend identified in NC meteorites

277 is due to two endmembers produced by thermal processing under different conditions, while Spitzer et

278 al. (2020) invoke the incorporation of an "inclusion-like" reservoir enriched in *s*-process to the NC

279 reservoir. The two models are possible and not mutually exclusive, but a thermal processing origin

280 appears more likely (Yokoyama et al., 2019). In conclusion, the temporal distribution of Nd, Zr, Ba and

281 Mo isotope compositions is associated with a significant thermal processing event that destroyed up to

282 2 % of the material in the inner protoplanetary disc, based on refractory lithophile elements systematics.
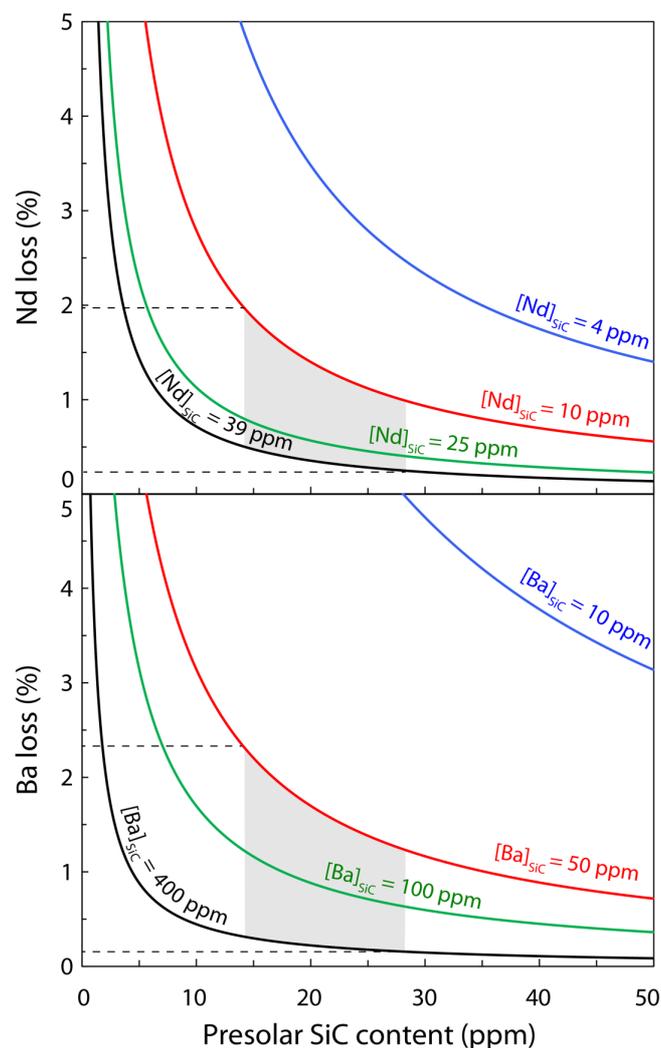
283

284 Figure 5: Nd and Ba fractions of the solar reservoir (in %) that is lost to account for the difference in
285 μ^{148}Nd and μ^{135}Ba between achondrites and the Earth as a function of the presolar SiC content in the
286 bulk initial solar reservoir (in ppm). Achondrite compositions used here are the mean achondrite
287 composition for Nd and Juvinas eucrite measurement for Ba with μ^{135}Ba = 5 ± 4. (Andreasen and
288 Sharma, 2007). The various concentrations correspond to maximum concentrations measured in
289 presolar SiC (black curve), intermediate (green and red) and minimum concentrations (blue) inferred

290 from individual grains and bulk SiC separates (see Supplementary Information). Minimum Nd and Ba
291 concentrations are unlikely to represent the bulk presolar SiC composition. The grey area corresponds
292 to the likely range for Nd and Ba loss and presolar SiC content inferred from Ne isotope composition in
293 Orgueil (Huss and Lewis, 1995). The most accepted content of presolar SiC is 14.2 ± 0.8 ppm.

294 4.4   Major change in the inner solar system reservoir Nd isotope composition around 1.5 Ma

295 The shift in Nd isotope composition explained by thermal processing appears to have occurred around

296 1.5 Ma. The lack of trend between ages of accretion and nucleosynthetic anomalies suggests that thermal

297 processing was not protracted (Figure 4). This event may coincide with the main recorded period of

298 chondrule formation starting at ~1.6 Ma after CAI formation, and lasted about 2 million years (Pape et

299 al., 2019). Chondrules were ubiquitous within an inner portion of the protoplanetary disc as evidenced

300 by their presence in different chondrite groups and with different chemical and isotopic compositions.

301 They formed from diverse precursors during brief heating events in the protoplanetary disc while it was

302 still rich in gas (Galy et al., 2000). Chondrule formation involved temperatures up to 1850°C and cooling

303 rates from 100 to 1000°C/h (Hewins et al., 2005). Chondrule formation mechanisms are still debated

304 (Russell et al. 2018 for a recent review) but their formation conditions were likely to result in the

305 destruction of ISM dust in the surrounding medium. Escape of the gas from the system is needed to

306 explain the loss of Nd which is possible by the decoupling of gas and dust in the protoplanetary disc.

307 Whereas it is possible that chondrules formed before the chondrule-forming event recorded in

308 chondrites, it is likely that their ubiquity in chondrites reflects a large-scale transformation in the

309 protoplanetary disc. The change in nucleosynthetic anomalies in Nd and other systematics of the NC

310 reservoir is coincidental to chondrule formation recorded in chondrites (Figure 6). Although it may not

311 be strictly related to the thermal processing event, their contemporaneity is striking. Moreover, the

312 similar Nd nucleosynthetic composition of CC achondrites (Tafassasset and NWA 6704) and chondrites

313 could arise from the lower chondrule formation efficiency in the carbonaceous reservoir suggested by

314 the lower chondrule to matrix ratio in these meteorites (Krot et al., 2014).
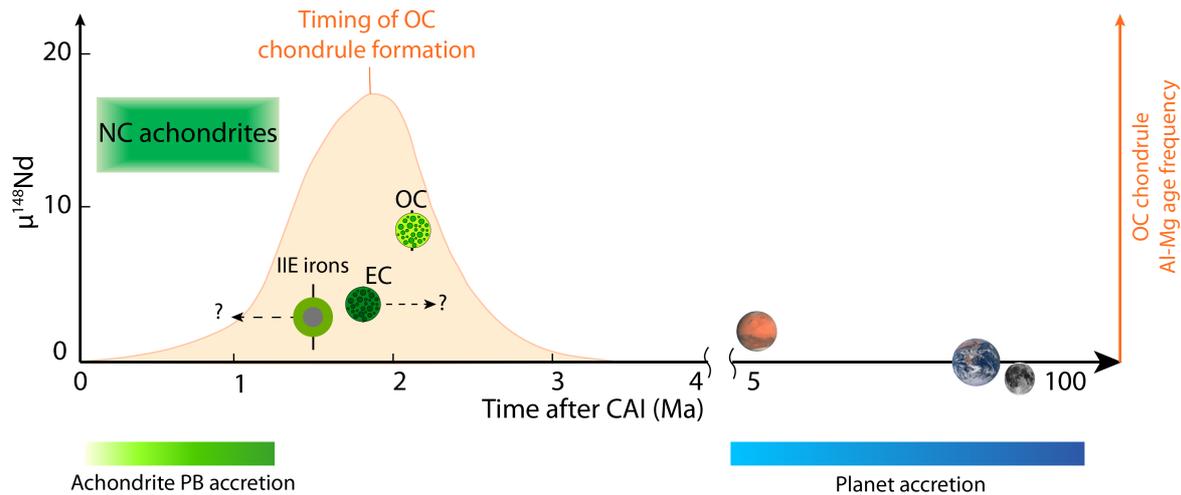
Figure 6: Sketch of the temporal evolution of the μ^{148}Nd composition of the planetesimals and planets and the ordinary chondrite (OC) chondrule Al-Mg age frequency (from Gregory et al., 2020). PB=parent body. During the first million year or so after CAI formation, the μ^{148}Nd of the planetesimals is relatively homogeneous and starts to decrease around 1.5 Ma as evidenced by the silicate inclusion of a IIE iron meteorite composition. This change in the isotope composition of inner solar system materials coincides with the chondrule formation recorded in OC chondrites (light orange). As discussed in the text, chondrule formation for EC is poorly constrained and might have happened later that for OC. Planets formed later and accreted various material including chondrites. Mars accreted before 10 Ma after CAI (e.g. Dauphas and Pourmand, 2011; Kruijer et al., 2020) while Earth's accretion continued until the Moon-forming impact dated between 30-250 Ma after CAI (Carlson et al., 2014).

4.5   Implications for terrestrial planets building blocks

Planets accreted over a long time period and likely incorporated large planetesimals during the process as well as chondrites (Raymond and Morbidelli, 2020 for a review). In the light of the reported Nd isotope composition of achondrites, the building blocks of terrestrial planets are reassessed qualitatively for refractory elements.

Earth's composition is an endmember for many isotopic systematics (Mezger et al., 2020). Mars' Nd isotope composition is identical to Earth's within errors, but is distinguishable for other elements such as O, Cr or Ti (Dauphas, 2017). Terrestrial planets accreted differently. For instance, Mars formed more rapidly than the Earth, as inferred from its size and formation age (Dauphas and Pourmand, 2011; Kruijer et al., 2020a). Mars may have thus incorporated different or less chondrite-like material than Earth and/or its building blocks may have been less affected by thermal processing, such as early planetesimals.

339 Earth's building blocks have been deduced from the isotope composition of chondrites and generally

340 agree with a major contribution of enstatite chondrites (Dauphas, 2017). The Nd isotope composition of

341 the Earth has been matched by only one meteorite sub-type so far: the EL3 enstatite chondrites (Boyet

342 et al., 2018). Schiller et al. (2020) propose that a large proportion of Earth's building blocks (~40 %) is

343 made of CI-like material, arguing that the μ^{48}Ca and μ^{54}Fe composition of meteorites are best explained

344 by mixing of an inner solar system component and a CI-like component. Despite having no

345 nucleosynthetic anomalies compared to Earth's composition on the stable isotopes of Nd, CI chondrites

346 display a deficit between -12 to -21 ppm in μ^{142}Nd. If this signature reflects a *p*-process deficit, it should

347 be recorded in the terrestrial μ^{144}Sm (pure *p*-process isotope), which is not the case (Bouvier et Boyet,

348 2016; Burkhardt et al., 2016). Concerning refractory lithophile elements, Earth's building blocks are

349 therefore potentially chiefly related to enstatite chondrites and most likely to EL3 chondrites (Boyet et

350 al., 2018).

351 The incorporation of early planetesimals in Earth's building blocks is another possibility. This scenario

352 has been suggested by Morbidelli et al. (2020) to explain Earth's Al/Si and Mg/Si ratios. More thermally

353 processed material is, however, necessary to balance Earth's composition considering a significant

354 contribution of early planetesimals with elevated $\mu^{145,148}$Nd in Earth's building blocks. Burkhardt et al.

355 (2016) proposed the existence of such an endmember, distinct from any kind of meteoritic material in

356 our collections. Recently reported isotope composition of highly siderophile Ru of ancient terrestrial

357 rocks formed before 3.8 Ga indicate that early Earth composition was distinct from all known meteorites

358 analysed so far (Fischer-Gödde et al., 2020). Assuming a similar distribution of the Nd and Ru

359 anomalies, these results favour the second scenario, namely that Earth's composition is an endmember

360 different from any chondritic (or known) material. Nucleosynthetic anomalies are however significantly

361 related to the behaviour of the carriers of the anomalies in different environments (e.g. Worsham et al.,

362 2019). In this scenario, Earth would have accreted a large proportion of early planetesimals mixed with

363 material more thermally processed than chondrites and more enriched in *s*-process.

364

Conclusions

Various carbonaceous and non-carbonaceous achondrites samples were analysed for mass-independent Nd isotope composition. Tafassasset and NWA 6704 carbonaceous achondrites have a similar Nd composition to the CR chondrites group from which they are possibly spatially related. The NC achondrites including aubrites, eucrites, ureilites, ungrouped meteorites, as well as angrites from this study and the literature display anomalies μ^{145}Nd and μ^{148}Nd between + 3.9 and + 11.0 ppm and + 9.1 and + 17.9 ppm respectively. The NC achondrites are distinct from NC chondrites and lie between ordinary and carbonaceous chondrite compositions. Planetary bodies (Earth, Mars and the Moon) as well as IIE irons display smaller anomalies μ^{145}Nd and μ^{148}Nd between + 0.4 and + 4.4 ppm and - 1.8 and 4.3 ppm respectively, undistinguishable within errors.

The redox conditions of achondrites used as a proxy for the heliocentric distance shows that NC achondrites sample parent bodies formed in different location of the solar system have a similar Nd isotope composition. This suggests that the difference in composition observed between NC achondrites and chondrites is not related to the heliocentric distance. Early planetesimals achondrites accreted earlier than chondrites, most likely before 1.5 Ma as inferred from the IIE irons accretion age. Altogether, this suggests a time-related origin of the Nd nucleosynthetic anomalies distribution in the inner solar system. This trend is also identified in other isotopic systematics such as those of Mo and Zr.

Thermal processing is the more likely process to produce the variations in Nd isotope composition within 1.5 Myr after the formation of CAI. The dust in the protoplanetary disc is more prone to be destroyed than the carriers of *s*-process isotopes such highly refractory SiC. Moreover, mass balance calculations show that up to 2 % of the Nd mass needs to be destroyed between the accretion of early achondrite parent bodies and terrestrial planets. The timing of this event coincides with chondrule formation. Achondrite compositions show that a thermal processing event within 1.5 Myr was a landmark of the inner solar system evolution and influenced the terrestrial planet composition.

404   Akram, W., Schönbächler, M., Bisterzo, S., & Gallino, R., 2015. Zirconium isotope evidence for the

405   heterogeneous distribution of s-process materials in the solar system. Geochimica et

406   Cosmochimica Acta, 165, 484-500.

407   Andreasen, R., Sharma, M., 2007. Mixing and Homogenization in the Early Solar System: Clues from

408   Sr, Ba, Nd, and Sm Isotopes in Meteorites. The Astrophysical Journal 665, 874–883.

409   https://doi.org/10.1086/518819

410   Bisterzo, S., Travaglio, C., Gallino, R., Wiescher, M., & Käppeler, F., 2014. Galactic chemical evolution

411   and solar s-process abundances: Dependence on the ^{13}C-pocket structure. The Astrophysical

412   Journal 787, 10.

413   Blichert-Toft, J., Göpel, C., Chaussidon, M., Albarède, F., 2020. Th/U variability in Allende chondrules.

414   Geochimica et Cosmochimica Acta 280, 378–394. https://doi.org/10.1016/j.gca.2020.04.006

415   Bollard, J., Connelly, J.N., Whitehouse, M.J., Pringle, E.A., Bonal, L., Jørgensen, J.K., Nordlund, Å.,

416   Moynier, F., Bizzarro, M., 2017. Early formation of planetary building blocks inferred from Pb

417   isotopic ages of chondrules. Sci. Adv. 3, e1700407. https://doi.org/10.1126/sciadv.1700407

418   Boss, A.P., 1998. Temperatures in protoplanetary disks. Annu. Rev. Earth Planet. Sci. 26, 53–80.

419   https://doi.org/10.1146/annurev.earth.26.1.53

420   Boss, A. P., & Goswami, J. N. (2006). Presolar cloud collapse and the formation and early evolution of

421   the solar nebula. Meteorites and the early solar system II, 171-186.

422   Bouvier, A., Vervoort, J.D., Patchett, P.J., 2008. The Lu-Hf and Sm-Nd isotopic composition of CHUR:

423   constraints from unequilibrated chondrites and implications for the bulk composition of terrestrial

424   planets. Earth and Planetary Science Letters 273, 48-57.

425   Bouvier, A., Boyet, M., 2016. Primitive Solar System materials and Earth share a common initial ^{142}Nd

426   abundance. Nature 537, 399–402.

427   Boyet, M., Bouvier, A., Frossard, P., Hammouda, T., Garçon, M., Gannoun, A., 2018. Enstatite

428   chondrites EL3 as building blocks for the Earth: The debate over the ^{146}Sm–^{142}Nd systematics.

429   Earth and Planetary Science Letters 488, 68–78. https://doi.org/10.1016/j.epsl.2018.02.004

430   Boyet, M., Carlson, R.W., 2005. ^{142}Nd evidence for early (> 4.53 Ga) global differentiation of the silicate

431   Earth. Science 309, 576–581.

432   Boyet, M., Gannoun, A., 2013. Nucleosynthetic Nd isotope anomalies in primitive enstatite chondrites.

433   Geochimica et Cosmochimica Acta 121, 652–666. https://doi.org/10.1016/j.gca.2013.07.036

434   Budde, G., Burkhardt, C., Kleine, T., 2019. Molybdenum isotopic evidence for the late accretion of

435   outer Solar System material to Earth. Nat Astron 3, 736–741. https://doi.org/10.1038/s41550-

436   019-0779-y

437   Burkhardt, C., Borg, L., Brennecka, G., Shollenberger, Q., Dauphas, N., Kleine, T., 2016. A

438   nucleosynthetic origin for the Earth's anomalous ^{142}Nd composition. Nature 537, 394–398.

439   Burkhardt, C., Dauphas, N., Tang, H., Fischer-Gödde, M., Qin, L., Chen, J.H., Rout, S.S., Pack, A.,
440   Heck, P.R., Papanastassiou, D.A., 2017. In search of the Earth-forming reservoir: Mineralogical,
441   chemical, and isotopic characterizations of the ungrouped achondrite NWA 5363/NWA 5400 and
442   selected chondrites. Meteoritics & Planetary Science 52, 807–826.

443   Carlson, R. W., Borg, L. E., Gaffney, A. M., & Boyet, M. (2014). Rb-Sr, Sm-Nd and Lu-Hf isotope
444   systematics of the lunar Mg-suite: the age of the lunar crust and its relation to the time of Moon
445   formation. Philosophical Transactions of the Royal Society A: Mathematical, Physical and
446   Engineering Sciences, 372(2024), 20130246.

447   Dauphas, N., 2017. The isotopic nature of the Earth's accreting material through time. Nature 541, 521–
448   524.

449   Dauphas, N., Pourmand, A., 2011. Hf-W-Th evidence for rapid growth of Mars and its status as a
450   planetary embryo. Nature 473, 489–492.

451   Dauphas, N., Remusat, L., Chen, J.H., Roskosz, M., Papanastassiou, D.A., Stodolna, J., Guan, Y., Ma,
452   C., Eiler, J.M., 2010. Neutron-rich chromium isotope anomalies in supernova nanoparticles. ApJ
453   720, 1577–1591. https://doi.org/10.1088/0004-637X/720/2/1577

454   Desch, S. J., Kalyaan, A., & Alexander, C. M. O'D., 2018. The effect of Jupiter's formation on the
455   distribution of refractory elements and inclusions in meteorites. The Astrophysical Journal
456   Supplement Series 238, 11.

457   DeMeo, F.E., Carry, B., 2014. Solar System evolution from compositional mapping of the asteroid belt.
458   Nature 505, 629–634. https://doi.org/10.1038/nature12908

459   Ek, M., Hunt, A. C., Lugaro, M., & Schönbächler, M., 2020. The origin of s-process isotope
460   heterogeneity in the solar protoplanetary disk. Nature Astronomy, 4, 273-281.

461   Fischer-Gödde, M., Kleine, T., 2017. Ruthenium isotopic evidence for an inner Solar System origin of
462   the late veneer. Nature 541, 525-527.

463   Fischer-Gödde, M., Elfers, B.-M., Münker, C., Szilas, K., Maier, W.D., Messling, N., Morishita, T.,

464   Van Kranendonk, M., Smithies, H., 2020. Ruthenium isotope vestige of Earth's pre-late-veneer mantle

465   preserved in Archaean rocks. Nature 579, 240–244. https://doi.org/10.1038/s41586-020-2069-3

466   Fukai, R., Yokoyama, T., 2017. Neodymium isotope heterogeneity of ordinary and carbonaceous

467   chondrites and the origin of non-chondritic [142]Nd compositions in the Earth. Earth and Planetary Science

468   Letters 474, 206–214. https://doi.org/10.1016/j.epsl.2017.06.036

469   Galy, A., Young, E.D., Ash, R.D., O'Nions, R.K., 2000. The formation of chondrules at high gas
470   pressures in the solar nebula. Science 290, 1751–1753.

471   Garçon, M., Boyet, M., Carlson, R.W., Horan, M.F., Auclair, D., Mock, T.D., 2018. Factors influencing
472   the precision and accuracy of Nd isotope measurements by thermal ionization mass spectrometry.
473   Chemical Geology 476, 493–514. https://doi.org/10.1016/j.chemgeo.2017.12.003

474   Gardner-Vandy, K. G., Lauretta, D. S., Greenwood, R. C., McCoy, T. J., Killgore, M., & Franchi, I. A.,

475   2012. The Tafassasset primitive achondrite: Insights into initial stages of planetary differentiation.

476   Geochimica et Cosmochimica Acta, 85, 142-159.

477   Gregory, T., Luu, T. H., Coath, C. D., Russell, S. S., & Elliott, T., 2020. Primordial formation of major

478   silicates in a protoplanetary disc with homogeneous $^{26}Al/^{27}Al$. Science advances 6, eaay9626.

479   Grossman, L., Beckett, J.R., Fedkin, A.V., Simon, S.B., Ciesla, F.J., 2008. Redox Conditions in the

480   Solar Nebula: Observational, Experimental, and Theoretical Constraints. Reviews in Mineralogy

481   and Geochemistry 68, 93–140. https://doi.org/10.2138/rmg.2008.68.7

482   Hewins, R., Connolly, H., Lofgren Jr, G., Libourel, G., 2005. Experimental constraints on chondrule

483   formation. Presented at the Chondrites and the protoplanetary disk, p. 286.

484   Hibiya, Y., Archer, G. J., Tanaka, R., Sanborn, M. E., Sato, Y., Iizuka, T., ... & Nakamura, T., 2019.

485   The origin of the unique achondrite Northwest Africa 6704: Constraints from petrology,

486   chemistry and Re–Os, O and Ti isotope systematics. Geochimica et cosmochimica acta, 245, 597-

487   627.

488   Hilton, C.D., Walker, R.J., 2020. New implications for the origin of the IAB main group iron meteorites

489   and the isotopic evolution of the noncarbonaceous (NC) reservoir. Earth and Planetary Science

490   Letters 540, 116248. https://doi.org/10.1016/j.epsl.2020.116248

491   Hoppe, P., Ott, U., 1997. Mainstream silicon carbide grains from meteorites. AIP Conference

492   Proceedings 402, 27–58. https://doi.org/10.1063/1.53314

493   Hunt, A. C., Cook, D. L., Lichtenberg, T., Reger, P. M., Ek, M., Golabek, G. J., & Schönbächler, M.,

494   2018. Late metal–silicate separation on the IAB parent asteroid: constraints from combined W

495   and Pt isotopes and thermal modelling. Earth and Planetary Science Letters, 482, 490-500.

496   Huss, G.R., 1997. The survival of presolar grains in solar system bodies, in: Astrophysical Implications

497   of the Laboratory Study of Presolar Materials. Presented at the Astrophysical Implications Of The

498   Laboratory Study Of Presolar Materials, Asce, St. Louis, Missouri (USA), pp. 721–748.

499   https://doi.org/10.1063/1.53338

500   Huss, G.R., Lewis, R.S., 1995. Presolar diamond, SiC, and graphite in primitive chondrites: Abundances

501   as a function of meteorite class and petrologic type. Geochimica et Cosmochimica Acta 59, 115–

502   160.

503   A.N. Krot, K. Keil, E.R.D. Scott, C.A. Goodrich, M.K. Weisberg, 2014. "1.1 - Classification of

504   Meteorites and Their Genetic Relationships" Editor(s): Heinrich D. Holland, Karl K. Turekian,

505   Treatise on Geochemistry (Second Edition), Elsevier. 1-63.

506 Kruijer, T.S., Borg, L.E., Wimpenny, J., Sio, C.K., 2020a. Onset of magma ocean solidification on Mars
507 inferred from Mn-Cr chronometry. Earth and Planetary Science Letters 542, 116315.
508 https://doi.org/10.1016/j.epsl.2020.116315

509 Kruijer, T.S., Burkhardt, C., Budde, G., Kleine, T., 2017. Age of Jupiter inferred from the distinct
510 genetics and formation times of meteorites. Proc Natl Acad Sci USA 114, 6712-6716.
511 https://doi.org/10.1073/pnas.1704461114

512 Kruijer, T.S., Kleine, T., 2019. Age and origin of IIE iron meteorites inferred from Hf-W chronology.
513 Geochimica et Cosmochimica Acta 262, 92–103. https://doi.org/10.1016/j.gca.2019.07.039

514 Kruijer, T.S., Kleine, T., Borg, L.E., 2020b. The great isotopic dichotomy of the early Solar System.
515 Nat Astron 4, 32–40. https://doi.org/10.1038/s41550-019-0959-9

516 Leya, I., Schönbächler, M., Wiechert, U., Krähenbühl, U., & Halliday, A. N., 2008. Titanium isotopes
517 and the radial heterogeneity of the solar system. Earth and Planetary Science Letters, 266, 233-
518 244.

519 Le Guillou, C., Changela, H.G., Brearley, A.J., 2015. Widespread oxidized and hydrated amorphous
520 silicates in CR chondrites matrices: Implications for alteration conditions and H_2 degassing of
521 asteroids. Earth and Planetary Science Letters 420, 162–173.
522 https://doi.org/10.1016/j.epsl.2015.02.031

523 Mahan, B., Moynier, F., Siebert, J., Gueguen, B., Agranier, A., Pringle, E.A., Bollard, J., Connelly, J.N.,
524 Bizzarro, M., 2018. Volatile element evolution of chondrules through time. Proc Natl Acad Sci
525 USA 115, 8547–8552. https://doi.org/10.1073/pnas.1807263115

526 Mezger, K., Schönbächler, M., Bouvier, A., 2020. Accretion of the Earth—Missing Components? Space
527 Sci Rev 216, 27. https://doi.org/10.1007/s11214-020-00649-y

528 Morbidelli, A., Lunine, J. I., O'Brien, D. P., Raymond, S. N., & Walsh, K. J.,2012. Building terrestrial
529 planets. Annual Review of Earth and Planetary Sciences 40, 251-275.

530 Morbidelli, A., Libourel, G., Palme, H., Jacobson, S.A., Rubie, D.C., 2020. Subsolar Al/Si and Mg/Si
531 ratios of non-carbonaceous chondrites reveal planetesimal formation during early condensation
532 in the protoplanetary disk. Earth and Planetary Science Letters 538, 116220.
533 https://doi.org/10.1016/j.epsl.2020.116220

534 Nagashima, K., Kita, N. T. and Luu, T.-H., 2018. "[26]Al–[26]Mg Systematics of Chondrules" in Russell, S.
535 S., Connolly Jr., H. C., and Krot, A. N. (eds) Chondrules: Records of Protoplanetary Disk
536 Processes. Cambridge: Cambridge University Press (Cambridge Planetary Science), pp. 247–275.
537 doi: 10.1017/9781108284073.009.

538 Nanne, J.A.M., Nimmo, F., Cuzzi, J.N., & Kleine, T. (2019). Origin of the non-carbonaceous–
539 carbonaceous meteorite dichotomy. Earth and Planetary Science Letters, 511, 44-54.

540 Pape, J., Mezger, K., Bouvier, A.-S., Baumgartner, L.P., 2019. Time and duration of chondrule
541   formation: Constraints from ^{26}Al-^{26}Mg ages of individual chondrules. Geochimica et
542   Cosmochimica Acta 244, 416–436. https://doi.org/10.1016/j.gca.2018.10.017

543 Qin, L., Carlson, R.W., Alexander, C.M., 2011a. Correlated nucleosynthetic isotopic variability in Cr,
544   Sr, Ba, Sm, Nd and Hf in Murchison and QUE 97008. Geochimica et Cosmochimica Acta 75,
545   7806–7828.

546 Qin, L., Nittler, L.R., Alexander, C.M.O., Wang, J., Stadermann, F.J., Carlson, R.W., 2011b. Extreme
547   ^{54}Cr-rich nano-oxides in the CI chondrite Orgueil – Implication for a late supernova injection into
548   the   solar   system.   Geochimica   et   Cosmochimica   Acta   75,   629–644.
549   https://doi.org/10.1016/j.gca.2010.10.017

550 Raymond, S.N., Morbidelli, A. Planet formation: key mechanisms and global models. Lecture Notes of
551   the 3rd Advanced School on Exoplanetary Science (Eds. Mancini, Biazzo, Bozza, Sozzetti).
552   arXiv:2002.05756

553 Render, J., Fischer-Gödde, M., Burkhardt, C., Kleine, T., 2017. The cosmic molybdenum-neodymium
554   isotope correlation and the building material of the Earth. Geochemical Perspectives Letters 3,
555   170-178.

556 Render, J., & Brennecka, G. A., 2021. Isotopic signatures as tools to reconstruct the primordial
557   architecture of the Solar System. Earth and Planetary Science Letters 555, 116705.

558 Righter, K., Sutton, S. R., Danielson, L., Pando, K., & Newville, M., 2016. Redox variations in the inner
559   solar system with new constraints from vanadium XANES in spinels. American Mineralogist,
560   101, 1928-1942.

561 Russell, S.S., Connolly Jr, H.C., & Krot, A.N. (Eds.)., 2018. Chondrules: Records of Protoplanetary
562   Disk Processes. Cambridge University Press, p. 467.

563 Saji, N. S., Wielandt, D., Holst, J. C., Bizzarro, M., 2020. Solar system Nd isotope heterogeneity:
564   Insights into nucleosynthetic components and protoplanetary disk evolution. Geochimica et
565   Cosmochimica Acta 281, 135-148.

566 Sanborn, M. E., Wimpenny, J., Williams, C. D., Yamakawa, A., Amelin, Y., Irving, A. J., & Yin, Q. Z.,
567   2019. Carbonaceous achondrites Northwest Africa 6704/6693: Milestones for early Solar System
568   chronology and genealogy. Geochimica et Cosmochimica Acta, 245, 577-596.

569 Schiller, M., Bizzarro, M., Fernandes, V.A., 2018. Isotopic evolution of the protoplanetary disk and the
570   building   blocks   of   Earth   and   the   Moon.   Nature   555,   507–510.
571   https://doi.org/10.1038/nature25990

572 Schiller, M., Bizzarro, M., Siebert, J., 2020. Iron isotope evidence for very rapid accretion and
573   differentiation of the proto-Earth. Sci. Adv. 6, eaay7604. https://doi.org/10.1126/sciadv.aay7604

574   Scott, E.R.D., Krot, A.N., 2005. Thermal Processing of Silicate Dust in the Solar Nebula: Clues from
575   Primitive Chondrite Matrices. ApJ 623, 571–578. https://doi.org/10.1086/428606

576   Srinivasan, P., Dunlap, D.R., Agee, C.B., Wadhwa, M., Coleff, D., Ziegler, K., Zeigler, R., McCubbin,
577   F.M., 2018. Silica-rich volcanism in the early solar system dated at 4.565 Ga. Nature
578   communications 9, 3036.

579   Spitzer, F., Burkhardt, C., Budde, G., Kruijer, T.S., Morbidelli, A., Kleine, T., 2020. Isotopic evolution
580   of the inner solar system inferred from molybdenum isotopes in meteorites. ApJ 898, L2.

581   Stephan, T., Trappitsch, R., Hoppe, P., Davis, A. M., Pellin, M. J., & Pardo, O. S., 2019. Molybdenum
582   Isotopes in Presolar Silicon Carbide Grains: Details of s-process Nucleosynthesis in Parent Stars
583   and Implications for r-and p-processes. The Astrophysical Journal, 877, 101.

584   Sugiura, N., Fujiya, W., 2014. Correlated accretion ages and ε^{54}Cr of meteorite parent bodies and the
585   evolution   of   the   solar   nebula.   Meteorit   Planet   Sci   49,   772–787.
586   https://doi.org/10.1111/maps.12292

587   Tielens, A., Waters, L., Bernatowicz, T., 2005. Origin and evolution of dust in circumstellar and
588   interstellar environments. Presented at the Chondrites and the Protoplanetary Disk, p. 605.

589   Trinquier, A., Birck, J.-L., Allègre, C.J., 2007. Widespread ^{54}Cr heterogeneity in the inner solar system.
590   ApJ, 655, 1179-1185. https://doi.org/10.1086/510360

591   Worsham, E.A., Burkhardt, C., Budde, G., Fischer-Gödde, M., Kruijer, T.S., Kleine, T., 2019. Distinct
592   evolution of the carbonaceous and non-carbonaceous reservoirs: Insights from Ru, Mo, and W
593   isotopes.   Earth   and   Planetary   Science   Letters   521,   103–112.
594   https://doi.org/10.1016/j.epsl.2019.06.001

595   Yang, L., Ciesla, F.J., 2012. The effects of disk building on the distributions of refractory materials in
596   the solar nebula: Refractory objects transport in the solar nebula. Meteoritics & Planetary Science
597   47, 99–119. https://doi.org/10.1111/j.1945-5100.2011.01315.x

598   Yokoyama, T., Nagai, Y., Fukai, R., & Hirata, T., 2019. Origin and Evolution of Distinct Molybdenum
599   Isotopic Variabilities within Carbonaceous and Noncarbonaceous Reservoirs. The Astrophysical
600   Journal, 883, 62.

601   Zhu, K., Liu, J., Moynier, F., Qin, L., Alexander, C.M.O., He, Y., 2019. Chromium Isotopic Evidence
602   for an Early Formation of Chondrules from the Ornans CO Chondrite. ApJ 873, 82.
603   https://doi.org/10.3847/1538-4357/aafe79

604   Zinner E., 2014. Presolar Grains, in Treatise on Geochemistry (2nd edition), 181-213. Elsevier. H. D.
605   Holland, K. K. Turekian (Eds.).

Supplementary information

Evidence from achondrites for a temporal change in Nd nucleosynthetic anomalies within the first 1.5 million years of the inner solar system formation

Paul Frossard[1*], Zhiguo Guo[2], Mary Spencer[2], Maud Boyet[1], Audrey Bouvier[3, 2]

[1] Université Clermont Auvergne, CNRS, IRD, OPGC, Laboratoire Magmas et Volcans, F-63000 Clermont-Ferrand, France

[2] Department of Earth Sciences, University of Western Ontario, N6A 5B7 London, Ontario, Canada

[3] Bayerisches Geoinstitut, Universität Bayreuth, 95447 Bayreuth, Germany

*Corresponding author: paul.frossard@uca.fr

Table of contents

List of supplementary figures

Figure S1: Nd nucleosynthetic anomalies

Figure S2: Comparison of decay-corrected and theoretical μ^{142}Nd

List of supplementary tables

Included in this document

Table S1: Sm isotope composition of achondrites

Table S2: Nd and Sm isotope composition of the standards

Included in a spreadsheet

Table S3: Nd isotope composition of achondrites

Table S4: Nd isotope composition of martian meteorites

Table S5: Nd isotope composition of lunar samples

Table S6: Nd isotope composition of chondrites

Table S7: Zr isotope composition of meteorite groups

Table S8: Mo isotope composition of meteorite groups

Table S9: Cr isotope composition of meteorite groups

1. Sample information

2. Nd and Sm isotope dilution analyses

For isotopic dilution, enriched mixed ^{149}Sm-^{150}Nd spikes were added and homogenised overnight with the sample solutions prior to evaporation. Rare-Earth Elements (REE) were separated from the matrix using cation resin AG 50W-X8 200-400 mesh on separate columns dedicated for spiked and non-spiked samples respectively (see further details in Bouvier and Boyet, 2016). The Nd and Sm cuts from spiked samples were further separated on Ln-Spec 50-100 µm Eichrom® resin.

Spiked Nd and Sm fractions were analysed using a Thermo Scientific™ Neptune Plus multi-collector ICP-MS at LMV. Samples were uptaken in 0.05 M HNO_3 solution which was introduced using a desolvator CETAC Aridus system with Ar and N_2 gases added to control the oxide production in the plasma (see Bouvier and Boyet, 2016; Boyet et al., 2018 for more details). Neodymium and Sm samples were analysed in one block of 60 or 30 cycles respectively, each with an integration time of 8 seconds. All Nd compositions were normalised to ^{146}Nd/^{144}Nd=0.7219 using an exponential law to correct mass fractionation. JNdi-1 standards were analysed every 3 samples.

For Sm, there is no standard normalisation required for isotopic dilutions. Nevertheless, a Sm standard was analyzed at the beginning of the session to control the instrumental mass bias.

A USGS BCR-2 basalt rock standard was analysed to assess the external reproducibility and accuracy of our measurements and isotope dilution deconvolution, and yielded a composition within 0.2% of reported values (Boyet et al., 2018).

3. Sm isotope analyses

Samarium was separated from the other REE the cation resin AG 50W-X8 in 2-methylactic acid medium.

Samples were loaded in 2 M HNO_3 on outgassed zone-refined Re filaments and were analysed following the method described in Bouvier and Boyet (2016). The axial cup is centred on mass 149, while Nd and Gd interferences were monitored on masses 146 (L3) and 155 or 156 (H4), respectively. The external

reproducibility was evaluated using an Inorganic Ventures 1000 ppm ICP-MS Sm solution, which is 20-37 p.p.m. on $^{144}Sm/^{152}Sm$, 10-18 p.p.m. on $^{148}Sm/^{152}Sm$, 4-11 p.p.m. on $^{149}Sm/^{152}Sm$, 10-27 p.p.m. on $^{150}Sm/^{152}Sm$, and 10-25 p.p.m. on $^{154}Sm/^{152}Sm$ ratios. All Sm isotope compositions are normalised to $^{147}Sm/^{152}Sm = 0.56081$ to correct mass fractionation.

4. Neutron capture effects

Mass-independent stable isotopic variations of planetary materials provide a record of the distribution of nucleosynthetic anomalies but also other nuclear processes such as neutron capture effects. Neutrons produced by interaction of matter with high energy galactic cosmic rays are captured by isotopes according to their cross-section. Neodymium isotopes are generally not well affected by neutron capture compared to other elements. Nevertheless, high fluxes of neutrons over a long period of time can modify the Nd isotope compositions of meteorites and Apollo lunar samples (e.g. Rankenburg et al., 2006). Samarium isotopes can be used as a dosimeter to correct for neutron capture effects on Nd as ^{149}Sm has the largest cross section among the rare earth elements. The deficit in $^{149}Sm/^{152}Sm$ has to be larger than 6 ε (ε = 100 ppm) to produce deviations larger than the analytical uncertainty on $^{145}Nd/^{144}Nd$ of 3 ppm, the most affected ratio among Nd mass-independent stable isotopic ratios (see Borg et al., 2019, Figure 5). Nd isotope compositions are not corrected for neutron capture effects as $\varepsilon^{149}Sm$ are lower than -2.3 in samples from this study (Table S10). Samarium isotopes were not measured for the silicate inclusion of Miles. A $\varepsilon^{149}Sm$ of -0.44 ± 0.06 ε has been previously measured by Schulz et al. (2012) on Miles silicate inclusions and therefore negligible neutron capture effects on $^{142,145,148,150}Nd$ isotopes are expected. From the measured Nd isotope composition of Miles, we do not detect any neutron capture effects.
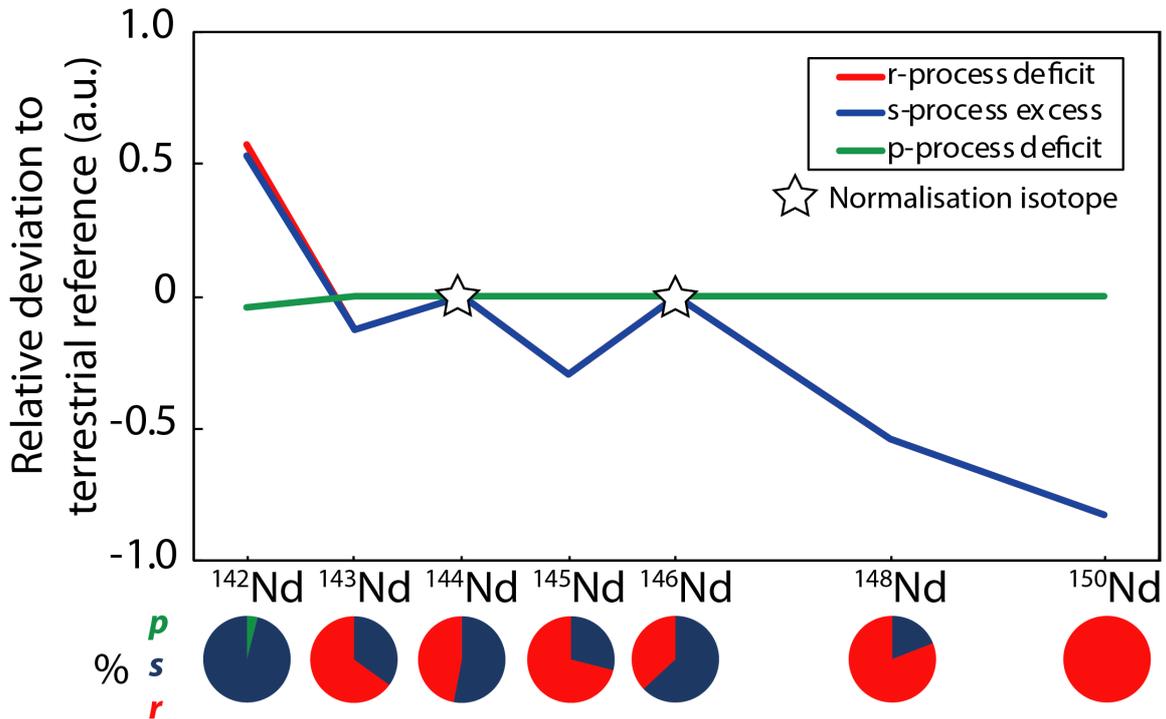
5. Nd nucleosynthetic anomalies

Figure S1: Theoretical deviations calculated relative to the terrestrial reference for excesses or deficits of nucleosynthetic processes with ratios normalised to ^{146}Nd/^{144}Nd ratio of 0.7219. Relative contributions of nucleosynthetic processes for each isotope are represented in sectors. Nucleosynthetic processes contributions are from Bisterzo et al. (2014).

6. Initial ^{142}Nd/^{144}Nd composition of the achondrites

Due to the decay of ^{146}Sm ($t_{1/2}$ = 103 Ma) into ^{142}Nd, the ^{142}Nd isotope composition of achondrites records differentiation events on planetesimals and reflects the Sm/Nd ratio of their source. Therefore, the measured ^{142}Nd/^{144}Nd ratio has to be corrected for the decay of ^{146}Sm. Concerning chondrites, two methods, hereafter A and B, have been used (see Boyet et al., 2018). Method A uses the precisely measured ^{147}Sm/^{144}Nd ratio of the samples to obtain the ^{142}Nd/^{144}Nd at the time of the Sm/Nd fractionation, considered as the formation of the solar system for chondrites, 4568 Ga ago (Bouvier and Wadhwa, 2010) and recalculate the ^{142}Nd/^{144}Nd at present time using the ^{147}Sm/^{144}Nd of the chondritic uniform reservoir (CHUR) of Bouvier et al. (2008). The method B uses the ^{143}Nd/^{144}Nd of the sample to recalculate the ^{147}Sm/^{144}Nd ratio of the sample that may be affected by terrestrial contamination, weathering or other recent perturbations that affect less significantly ^{143}Nd/^{144}Nd ratios. Then the same procedure is used to calculate the corrected the ^{142}Nd/^{144}Nd at present time. For differentiated meteorites, the time of Sm/Nd fractionation is inferred from ^{147}Sm-^{143}Nd systematics internal isochrons on samples or relying on other chronometers. We used both methods to correct the ^{142}Nd/^{144}Nd of achondrites samples and used Sm-Nd ages whenever available or Al-Mg and Pb-Pb ages instead. We note that other chronometers may be sensitive to different equilibration temperatures and therefore may not correspond well with the Sm/Nd fractionation event.

Many achondrites may have experienced a complex magmatic and metamorphic history, for example with several stages of Sm/Nd fractionation. This may be the case for complex crustal formation or impact processes on some parent bodies. The timing and extent of Sm/Nd fractionation at each stage cannot be accurately constrained and therefore leading to an erroneous corrected $^{142}Nd/^{144}Nd$. One way of assessing the accuracy of the corrected $^{142}Nd/^{144}Nd$ is the petrological study of the samples and trace element geochemistry of the minerals to assess whether they are at equilibrium with the adjacent minerals. Most meteorites included in this study were extensively studied (e.g. Tafassasset and NWA 6704 and pairs) and for most of them the systems seem undisturbed and reflect simple, one-stage evolution. Another way is to compare the corrected $^{142}Nd/^{144}Nd$ with a theoretical $^{142}Nd/^{144}Nd$ according to nucleosynthetic processes.

142-Neodymium is the only Nd isotope that was produced in part by the *p*-process. The proportion of the *p*-process contribution to 142-Nd is debated but ranges from 2 to 8 % in astrophysical calculations (Arlandini et al., 1999; Bisterzo et al., 2014) whereas some sample-based isotopic studies hypothesised contribution up to 20 % (Andreasen and Sharma, 2006; Gannoun et al., 2011). Such a large contribution of the *p*-process is however unlikely and may rather reflect s-process heterogeneity among chondrites as for other Nd isotopes (Bouvier and Boyet, 2016; Boyet et al., 2018; Burkhardt et al., 2016). One can calculate a theoretical $^{142}Nd/^{144}Nd$ using $^{145}Nd/^{144}Nd$ or $^{148}Nd/^{144}Nd$ ratios. The s-process mixing line can be defined using astrophysical models for nucleosynthesis, measuring the composition of the presolar SiC grains which are the main carrier of the *s*-process Nd in chondrites, and unequilibrated chondrite leachate regressions, but there is some discrepancy between these three estimates. Nucleosynthetic processes contribution for each isotopes are variable in astrophysical models and deviate from the measurements, notably on ^{146}Nd used for internal normalisation (Yin et al., 2006). Neodymium isotopes measurements on SiC are very difficult to perform and are obtained without elemental separation other than in the mass spectrometer, leading to large errors. The caveat with the leachate method is that it does not discriminate minerals individually and contains very little information on the nature of the anomalous carrier. However, leachates are obtained in the same conditions as the samples and are likely to represent the general trend on which the meteorite samples are scattered. Based on the leachate data on chondrites (Boyet and Gannoun, 2013; Qin et al., 2011) the $\mu^{142}Nd$ can be approximated to $-1.60 \times \mu^{145}Nd$ and $-0.915 \times \mu^{148}Nd$. The use of $\mu^{148}Nd$ is preferred because of the small range of variation in the $\mu^{145}Nd$ compared to the uncertainties associated.

Theoretical and corrected $\mu^{142}Nd$ using method B are compared in Figure S2. Most samples plot near the 1:1 line, but three samples are clearly offset. Miles silicate inclusion, martian meteorites and carbonaceous achondrites NWA 6704 and Tafassasset have initial $\mu^{142}Nd_B$ significantly different from $\mu^{142}Nd$ inferred from their $\mu^{148}Nd$ composition. Itqiy displays large errors but is not offset despite a high $^{147}Sm/^{144}Nd$ ratio, that reflects its high content in enstatite, and an extremely radiogenic composition in $^{143}Nd/^{144}Nd$ ($143 < \varepsilon^{143}Nd < 188$) and $\mu^{142}Nd$ ($313 < \mu^{142}Nd < 436$). The age of the Sm/Nd fractionation is not well defined with only an I-Xe age of -2.6 ± 2.6 Ma relative to the Shallowater aubrite standard

(Busfield et al., 2008; Gilmour and Crowther, 2017). An early event of differentiation and subsequent evolution could produce such a radiogenic composition with this Sm/Nd.

The deviation of the $\mu^{142}Nd_B$ from pure s-process nucleosynthetic anomalies in carbonaceous achondrites may be related to either a multi-stage evolution or p-process contribution. The former is unlikely as these rocks have been interpreted as melting products of a chondritic source (e.g. Gardner-Vandy et al., 2012; Hibiya et al., 2019). The contribution of the *p*-process will drag $\mu^{142}Nd$ down to more negative values, as observed in carbonaceous chondrites that contain p-depleted CAI (Bouvier and Boyet, 2016). This suggests that the reservoir from which carbonaceous achondrites formed was depleted in p-process and possibly contained CAI in order to produce this nucleosynthetic composition.
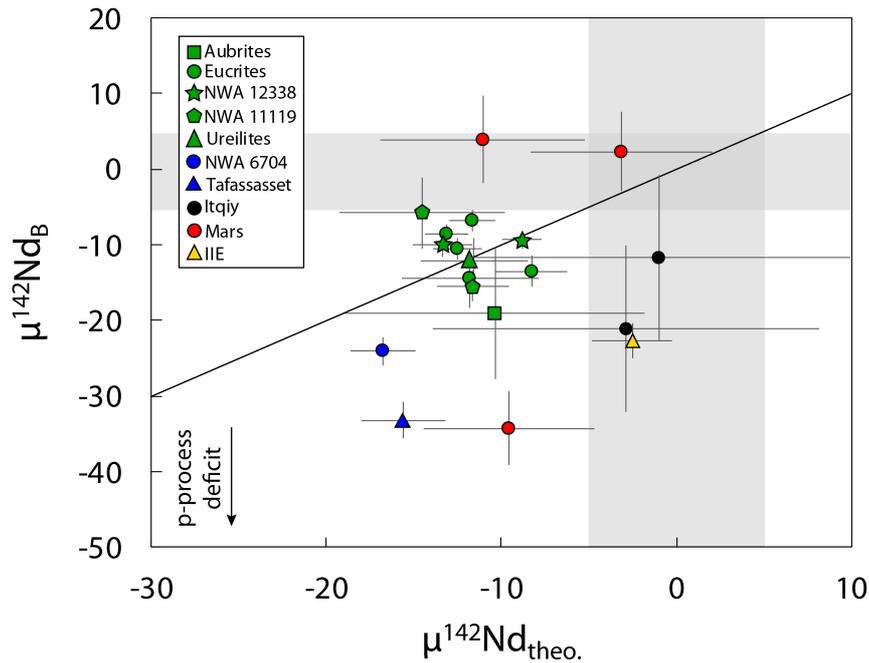

Figure S2: Comparison of theoretical $\mu^{142}Nd$ ($\mu^{142}Nd_{theo.}$) according to nucleosynthetic *s*-process, calculated using acid leachates regression (see text) and the corrected $\mu^{142}Nd$ calculated with method B ($\mu^{142}Nd_B$) of Boyet et al. (2018) using $^{143}Nd/^{144}Nd$ ratio. The grey areas represent the typical uncertainties on the standard measurements using the 4-lines dynamic method of Garçon et al. (2018).

7. References used for Nd isotope composition of achondrites and planetary bodies in Table 2

Angrites: Saji et al. (2020), Render and Brennecka (2021).

Eucrites: This study, Render and Brennecka (2021).

Bunburra Rockhole: Render and Brennecka (2021).

NWA 5363: Burkhardt et al. (2016).

Mars: Armytage et al. (2018), Borg et al. (2016), Caro et al., (2008), Debaille et al. (2007) and Kruijer et al. (2017) and Saji et al. (2020).

Moon: Boyet and Carlson (2007), Brandon et al. (2009), McLeod et al. (2014), Boyet et al. (2015) and Borg et al. (2019).

Enstatite chondrites: Burkhardt et al. (2016) and Saji et al. (2020).

Ordinary chondrites: Burkhardt et al. (2016), Fukai and Yokoyama (2017) and Saji et al. (2020).

Carbonaceous chondrites: Burkhardt et al. (2016), Fukai and Yokoyama (2017, 2019) and Saji et al. (2020).

CAI: Brennecka et al. (2013), Bouvier and Boyet (2016) and Burkhardt et al. (2016). Only "non-terrestrial" CAI were included, Bouvier and Boyet (2016) reported CAI (Allende 322 and 323, NWA 6991 B4) with a Nd nucleosynthetic composition similar to terrestrial standards.

Concerning chondrites, Adrian (H4) and NWA 2090 (CO3) are discarded because they appear highly fractionated and deviate from chondrites from their respective groups; see Fukai and Yokoyama (2017) for discussion. The mean composition of carbonaceous chondrites does not include CV chondrites because of the varying content in CAI that greatly affects their Nd isotope composition as well as CI chondrites and Tagish Lake that have a distinct composition from other CC groups.

Data for chondrites from the literature includes only those obtained using dynamic mass spectrometric measurements for the stable isotopes of Nd.

8. Mixing equations used to estimate the lost fraction of the solar reservoir

The original composition of the solar reservoir can be estimated by mass balance (Eq. 1) using CI chondrites. We consider that CI chondrites contain an unaltered presolar SiC content (Huss, 1997).

$$\mu^{148}Nd_{CI} = \frac{X_{SiC} \times [Nd]_{SiC} \times \mu^{148}Nd_{SiC} + (1 - X_{SiC}) \times [Nd]_{\odot} \times \mu^{148}Nd_{\odot}}{X_{SiC} \times [Nd]_{SiC} + (1 - X_{SiC}) \times [Nd]_{\odot}}$$

In this equation, X_{SiC} corresponds to the concentration of SiC in CI chondrites, which is equal to 14.2 ± 0.8 ppm or 28.5 ± 3.3 ppm using two methods of calculation (Huss and Lewis, 1995). $[Nd]_{SiC}$ corresponds to the Nd content in presolar SiC that ranges from 0.5 to 11 ppm (average of 4 ppm) on large individual SiC grains (Amari et al., 1995) to 25 to 39 ppm in bulk SiC separates (Zinner et al., 1991). $[Nd]_{\odot}$ is the Nd content in the solar reservoir as defined in the main text and calculated with mass balance using CI chondrites Nd concentration, 0.464 ppm (Barrat et al., 2012). Similarly $\mu^{148}Nd_{CI}$, $\mu^{148}Nd_{SiC}$ and $\mu^{148}Nd_{\odot}$ correspond to the Nd isotope composition of CI chondrites (Fukai and Yokoyama, 2019), SiC (Hoppe and Ott, 1997) and the solar reservoir, respectively.

The isotope composition of the solar reservoir is derived from Eq. 1.

$$\mu^{148}Nd_{\odot} = \frac{X_{SiC} \times [Nd]_{SiC} \times \left(\mu^{148}Nd_{CI} - \mu^{148}Nd_{SiC}\right) + [Nd]_{\odot}\left(\mu^{148}Nd_{CI} - X_{SiC}\right)}{[Nd]_{\odot} - X_{SiC}}$$

In the light of the temporal shift reported here, and considering thermal processing of the solar *r-/p-* process enriched reservoir, we can calculate how much of the later has to be destroyed to explain the composition of the terrestrial planets.

One can describe this system with two equations:

$$\mu^{148}Nd_{Ach} = \frac{X_{SiC_{Ach}} \times [Nd]_{SiC} \times \mu^{148}Nd_{SiC} + (1 - X_{SiC_{Ach}}) \times [Nd]_{\odot} \times \mu^{148}Nd_{\odot}}{X_{SiC_{Ach}} \times [Nd]_{SiC} + (1 - X_{SiC_{Ach}}) \times [Nd]_{\odot}}$$

$$\mu^{148}Nd_{Earth} = \frac{X_{SiC_{Earth}} \times [Nd]_{SiC} \times \mu^{148}Nd_{SiC} + (1 - X_{SiC_{Earth}}) \times [Nd]_{\odot} \times \mu^{148}Nd_{\odot}}{X_{SiC_{Earth}} \times [Nd]_{SiC} + (1 - X_{SiC_{Earth}}) \times [Nd]_{\odot}}$$

With $X_{SiC_{Ach}}$ and $X_{SiC_{Earth}}$ corresponding to the concentration of SiC in the achondrite and Earth accreted material. This proportion differs because of the thermal processing of the solar reservoir. They correspond to the mass of the SiC endmember M_{SiC}, that remains unchanged, over the total mass, $M_{tot_{Ach}}$ and $M_{tot_{Earth}}$, which decreases with increasing thermal processing in the disk.

$$X_{SiC_{Ach}} = \frac{M_{SiC}}{M_{tot_{Ach}}} \text{ and } X_{SiC_{Earth}} = \frac{M_{SiC}}{M_{tot_{Earth}}}$$

Hence,

$$1 - \frac{X_{SiC_{Ach}}}{X_{SiC_{Earth}}} = \frac{M_{tot_{Ach}} - M_{tot_{Earth}}}{M_{tot_{Ach}}} = L$$

L is the mass fraction of Nd in the solar reservoir that is lost during thermal processing between the early planetesimal stage to planets accretion.

The same equations can be used for Ba. [Ba]$_{CI}$ is 2.46 ppm (Barrat et al., 2012). Ba content in SiC is highly variable. Amari et al. (1995) report bulk separates of SiC Ba concentrations of 442-129 ppm (average of 215 ppm) and individual SiC concentrations of 0.6-509 ppm (average of 49 ppm), whereas Ávila et al. (2013) report 380 ppm on a bulk separate and 1.7-10.4 ppm (average of 5.9 ppm) in individual SiC grains. Barium isotope compositions are based on Orgueil for CI chondrites from Carlson et al. (2007), on Juvinas for achondrites from Andreasen and Sharma (2007) and on the mean of a single SiC composition from Liu et al. (2014).

Amari, S., Hoppe, P., Zinner, E., Lewis, R.S., 1995. Trace-element concentrations in single circumstellar silicon carbide grains from the Murchison meteorite. Meteoritics 30, 679–693. https://doi.org/10.1111/j.1945-5100.1995.tb01165.x

Andreasen, R., Sharma, M., 2007. Mixing and Homogenization in the Early Solar System: Clues from Sr, Ba, Nd, and Sm Isotopes in Meteorites. ApJ 665, 874–883. https://doi.org/10.1086/518819

Andreasen, R., Sharma, M., 2006. Solar nebula heterogeneity in p-process samarium and neodymium isotopes. Science 314, 806–809.

Arlandini, C., Käppeler, F., Wisshak, K., Gallino, R., Lugaro, M., Busso, M., Straniero, O., 1999. Neutron capture in low-mass asymptotic giant branch stars: cross sections and abundance signatures. The Astrophysical Journal 525, 886.

Armytage, R.M.G., Debaille, V., Brandon, A.D., Agee, C.B., 2018. A complex history of silicate differentiation of Mars from Nd and Hf isotopes in crustal breccia NWA 7034. Earth and Planetary Science Letters 502, 274–283. https://doi.org/10.1016/j.epsl.2018.08.013

Ávila, J.N., Ireland, T.R., Gyngard, F., Zinner, E., Mallmann, G., Lugaro, M., Holden, P., Amari, S., 2013. Ba isotopic compositions in stardust SiC grains from the Murchison meteorite: Insights into the stellar origins of large SiC grains. Geochimica et Cosmochimica Acta 120, 628–647. https://doi.org/10.1016/j.gca.2013.03.039

Barrat, J.A., Zanda, B., Moynier, F., Bollinger, C., Liorzou, C., Bayon, G., 2012. Geochemistry of CI chondrites: Major and trace elements, and Cu and Zn Isotopes. Geochimica et Cosmochimica Acta 83, 79–92. https://doi.org/10.1016/j.gca.2011.12.011

Bisterzo, S., Travaglio, C., Gallino, R., Wiescher, M., Käppeler, F., 2014. Galactic chemical evolution and solar s-process abundances: Dependence on the ^{13}C-pocket structure. The Astrophysical Journal 787, 10.

Borg, L.E., Brennecka, G.A., Symes, S.J.K., 2016. Accretion timescale and impact history of Mars deduced from the isotopic systematics of martian meteorites. Geochimica et Cosmochimica Acta 175, 150–167. https://doi.org/10.1016/j.gca.2015.12.002

Borg, L.E., Connelly, J.N., Boyet, M., Carlson, R.W., 2011. Chronological evidence that the Moon is either young or did not have a global magma ocean. Nature 477, 70–72. https://doi.org/10.1038/nature10328

Borg, L.E., Gaffney, A.M., Kruijer, T.S., Marks, N.A., Sio, C.K., Wimpenny, J., 2019. Isotopic evidence for a young lunar magma ocean. Earth and Planetary Science Letters 523, 115706. https://doi.org/10.1016/j.epsl.2019.07.008

Bouvier, A., Boyet, M., 2016. Primitive Solar System materials and Earth share a common initial ^{142}Nd abundance. Nature 537, 399–402.

Bouvier, A., Vervoort, J.D., Patchett, P.J., 2008. The Lu–Hf and Sm–Nd isotopic composition of CHUR: constraints from unequilibrated chondrites and implications for the bulk composition of terrestrial planets. Earth and Planetary Science Letters 273, 48–57.

Bouvier, A., Wadhwa, M., 2010. The age of the Solar System redefined by the oldest Pb-Pb age of a meteoritic inclusion. Nature geoscience 3, 637.

Boyet, M., Bouvier, A., Frossard, P., Hammouda, T., Garçon, M., Gannoun, A., 2018. Enstatite chondrites EL3 as building blocks for the Earth: The debate over the ^{146}Sm–^{142}Nd systematics. Earth and Planetary Science Letters 488, 68–78. https://doi.org/10.1016/j.epsl.2018.02.004

Boyet, M., Carlson, R.W., 2007. A highly depleted moon or a non-magma ocean origin for the lunar crust? Earth and Planetary Science Letters 262, 505–516. https://doi.org/10.1016/j.epsl.2007.08.009

Boyet, M., Gannoun, A., 2013. Nucleosynthetic Nd isotope anomalies in primitive enstatite chondrites. Geochimica et Cosmochimica Acta 121, 652–666.

Brandon, A.D., Lapen, T.J., Debaille, V., Beard, B.L., Rankenburg, K., Neal, C., 2009. Re-evaluating 142Nd/144Nd in lunar mare basalts with implications for the early evolution and bulk Sm/Nd of the Moon. Geochimica et Cosmochimica Acta 73, 6421–6445. https://doi.org/10.1016/j.gca.2009.07.015

Burkhardt, C., Borg, L., Brennecka, G., Shollenberger, Q., Dauphas, N., Kleine, T., 2016. A nucleosynthetic origin for the Earth's anomalous ^{142}Nd composition. Nature 537, 394–398.

Burkhardt, C., Dauphas, N., Tang, H., Fischer-Gödde, M., Qin, L., Chen, J.H., Rout, S.S., Pack, A., Heck, P.R., Papanastassiou, D.A., 2017. In search of the Earth-forming reservoir: Mineralogical, chemical, and isotopic characterizations of the ungrouped achondrite NWA 5363/NWA 5400 and selected chondrites. Meteoritics & Planetary Science 52, 807–826.

Busfield, A., Turner, G., Gilmour, J., 2008. Testing an integrated chronology: I-Xe analysis of enstatite meteorites and a eucrite. Meteoritics & Planetary Science 43, 883–897.

Carlson, R.W., Boyet, M., Horan, M., 2007. Chondrite barium, neodymium, and samarium isotopic heterogeneity and early earth differentiation. Science 316, 1175–1178.

Caro, G., Bourdon, B., Halliday, A.N., Quitté, G., 2008. Super-chondritic Sm/Nd ratios in Mars, the Earth and the Moon. Nature 452, 336–339. https://doi.org/10.1038/nature06760

Debaille, V., Brandon, A.D., Yin, Q.Z., Jacobsen, B., 2007. Coupled ^{142}Nd–^{143}Nd evidence for a protracted magma ocean in Mars. Nature 450, 525–528. https://doi.org/10.1038/nature06317

Fukai, R., Yokoyama, T., 2019. Nucleosynthetic Sr–Nd Isotope Correlations in Chondrites: Evidence for Nebular Thermal Processing and Dust Transportation in the Early Solar System. ApJ 879, 79. https://doi.org/10.3847/1538-4357/ab0e0d

Fukai, R., Yokoyama, T., 2017. Neodymium isotope heterogeneity of ordinary and carbonaceous chondrites and the origin of non-chondritic ^{142}Nd compositions in the Earth. Earth and Planetary Science Letters 474, 206–214. https://doi.org/10.1016/j.epsl.2017.06.036

Gannoun, A., Boyet, M., Rizo, H., El Goresy, A., 2011. 146Sm–142Nd systematics measured in enstatite chondrites reveals a heterogeneous distribution of ^{142}Nd in the solar nebula. Proceedings of the National Academy of Sciences 108, 7693–7697.

Gardner-Vandy, K.G., Lauretta, D.S., Greenwood, R.C., McCoy, T.J., Killgore, M., Franchi, I.A., 2012. The Tafassasset primitive achondrite: Insights into initial stages of planetary differentiation. Geochimica et Cosmochimica Acta 85, 142–159.

Gilmour, J., Crowther, S., 2017. The I-Xe chronometer and its constraints on the accretion and evolution of planetesimals. Geochemical Journal 51, 69–80.

Hibiya, Y., Archer, G.J., Tanaka, R., Sanborn, M.E., Sato, Y., Iizuka, T., Ozawa, K., Walker, R.J., Yamaguchi, A., Yin, Q.-Z., 2019. The origin of the unique achondrite Northwest Africa 6704: Constraints from petrology, chemistry and Re–Os, O and Ti isotope systematics. Geochimica et Cosmochimica Acta 245, 597–627.

Hoppe, P., Ott, U., 1997. Mainstream silicon carbide grains from meteorites. AIP Conference Proceedings 402, 27–58. https://doi.org/10.1063/1.53314

Huss, G.R., 1997. The survival of presolar grains in solar system bodies. in: AIP Conference Proceedings 402, 721–748. https://doi.org/10.1063/1.53338

Huss, G.R., Lewis, R.S., 1995. Presolar diamond, SiC, and graphite in primitive chondrites: Abundances as a function of meteorite class and petrologic type. Geochimica et Cosmochimica Acta 59, 115–160.

Kruijer, T.S., Kleine, T., Borg, L.E., Brennecka, G.A., Irving, A.J., Bischoff, A., Agee, C.B., 2017. The early differentiation of Mars inferred from Hf–W chronometry. Earth and Planetary Science Letters 474, 345–354. https://doi.org/10.1016/j.epsl.2017.06.047

Liu, N., Savina, M.R., Davis, A.M., Gallino, R., Straniero, O., Gyngard, F., Pellin, M.J., Willingham, D.G., Dauphas, N., Pignatari, M., Bisterzo, S., Cristallo, S., Herwig, F., 2014. Ba isotopic composition of mainstream silicon carbides from Murchison: constraints for *s*-process nucleosynthesis in Asymptotic Giant Branch stars. ApJ 786, 66. https://doi.org/10.1088/0004-637X/786/1/66

McLeod, C.L., Brandon, A.D., Armytage, R.M.G., 2014. Constraints on the formation age and evolution of the Moon from [142]Nd–[143]Nd systematics of Apollo 12 basalts. Earth and Planetary Science Letters 396, 179–189. https://doi.org/10.1016/j.epsl.2014.04.007

Qin, L., Carlson, R.W., Alexander, C.M., 2011. Correlated nucleosynthetic isotopic variability in Cr, Sr, Ba, Sm, Nd and Hf in Murchison and QUE 97008. Geochimica et Cosmochimica Acta 75, 7806–7828.

Rankenburg, K., Brandon, A., Neal, C., 2006. Neodymium isotope evidence for a chondritic composition of the Moon. Science 312, 1369–1372.

Saji, N.S., Wielandt, D., Holst, J.C., Bizzarro, M., 2020. Solar system Nd isotope heterogeneity: Insights into nucleosynthetic components and protoplanetary disk evolution. Geochimica et Cosmochimica Acta 281, 135–148. https://doi.org/10.1016/j.gca.2020.05.006

Schulz, T., Upadhyay, D., Münker, C., Mezger, K., 2012. Formation and exposure history of non-magmatic iron meteorites and winonaites: Clues from Sm and W isotopes. Geochimica et Cosmochimica Acta 85, 200–212. https://doi.org/10.1016/j.gca.2012.02.012

Yin, Q.-Z., Lee, C.-T.A., Ott, U., 2006. Signatures of the s-process in presolar silicon carbide grains: Barium through hafnium. The Astrophysical Journal 647, 676.

Zinner, E., Amari, S., Lewis, R.S., 1991. S-process Ba, Nd, and Sm in presolar SiC from the Murchison meteorite. ApJ 382, L47. https://doi.org/10.1086/186210

Table S1: Sm isotope compositions of the achondrite samples and rock standards.

	Classification	Serie	I ^{147}Sm (V)	μ^{144}Sm	2 SD	μ^{148}Sm	2 SD	μ^{149}Sm	2 SD	μ^{150}Sm	2 SD	μ^{154}Sm	2 SD	^{147}Sm/^{152}Sm	^{146}Nd/^{152}Sm	^{155}Gd/^{152}Sm	cycles
Ungrouped achondrites																	
NWA 6704	Achon-ung	2	0.34	-81.6	55.8	60.1	20.9	-66.0	16.6	391.6	23.4	-18.5	18.5		0.00506	0.00010	300
Tafassasset	Achon-ung	2	0.08	-114.8	189.2	-12.4	59.2	-223.2	53.4	356.2	87.3	-49.3	52.7		0.00037	0.00056	360
NWA 11119	Achon-ung	3	0.19	0	72	-11	25	-150	21	254	27	-90	24	0.5621	0.00027	0.00013	160
NWA 11119 MS1		3	0.8	219	89	17	31	-128	34	269	35	-64	33	0.5617	0.00229	0.00042	100
NWA 12338 (1)a		3	0.83	32	15	0	7	-26	6	50	7	-21	7	0.5629	0.00089	0.00000	340
Eucrites								**0**									
Tirhert (1)	Eucrite	1	1.97	26.3	14.5	-4.2	5.3	2.7	4.7	-6.2	6.6	-6.4	5.2	0.5639	0.00034	0.00002	500
NWA 11001 (1)a	Eucrite	2	1.54	26.9	13.8	0.9	6.8	-53.8	5.9	101.7	7.2	-14.1	6.6		0.00028	0.00003	540
NWA 11001 (1)b	Eucrite	2	0.96	6.8	10.6	-2.1	7.8	-54.2	6.4	106.1	8.8	12.8	8.2		0.00017	0.00000	540
NWA 11001 (2)	Eucrite	2	0.62	12.9	27.9	5.4	12.9	-23.8	11.0	69.3	15.0	-6.2	12.7		0.00052	0.00004	360
Enstatite achondrites								**0**									
Khor Temiki	Aubrite	1	0.47	808.9	1436.6	195.5	186.0	-194.0	166.5	447.7	95.0	-272.3	122.2	0.5627	0.00644	0.00161	320
Itqiy (1)	EH7	1	0.57	-55.9	62.3	16.3	14.2	-28.4	12.1	83.0	17.1	-14.8	12.5	0.5632	0.00108	0.00001	300
Itqiy (2)	EH7	1	0.76	-58.0	42.6	34.9	13.1	-25.8	10.3	112.1	15.0	13.3	10.5	0.5633	0.00631	0.00001	240
Standards																	
Sm ICP	n = 8	1		0.114976±4	31.2	0.420428±6	14.8	0.516847±2	4.1	0.275980±3	9.7	0.850792±9	10.4	0.5640			
Sm ICP	n = 5	2		0.114976±2	19.9	0.420443±4	10.3	0.516853±5	9.6	0.275995±7	27.1	0.850798±22	25.4				
Sm ICP	n = 12	3		0.114976±5	41.3	0.420442±5	12.5	0.516847±6	11.1	0.275995±4	15.8	0.850788±13	15.1	0.5663			

Table S2: Compilation for Nd and Sm standard measurements. Errors are 2 standard deviations (2SD). Each serie is associated to samples reported in Table 1 with different methods of analysis.

Neodymium	Number of analyses	$^{142}Nd/^{144}Nd$	±	$^{143}Nd/^{144}Nd$	±	$^{145}Nd/^{144}Nd$	±	$^{146}Nd/^{144}Nd$	$^{148}Nd/^{144}Nd$	±	$^{150}Nd/^{144}Nd$	±
Serie 1												
JNdi-1 - Static	n=8	1.141837 ± 5	4.3	0.512110 ± 3	6.1	0.348403 ± 2	5.4	0.7227	0.241584 ± 2	9.5	0.236455 ± 4	15.6
Serie 2												
JNdi-1 – Dyn 2L	n=11	1.141835 ± 7	5.9	0.512121 ± 1	1.8	0.348410 ± 1	2.3		0.241570 ± 1	4.3	0.236462 ± 5	21.0
JNdi-1 - Static	n=2	1.141834 ± 11	9.9	0.512102 ± 3	5.1	0.348406 ± 5	13.2	0.7212	0.241595 ± 2	6.4	0.236476 ± 8	33.6
Serie 3												
JNdi-1 – Dyn 4L	n=6	1.141829 ± 6	4.9	0.512098 ± 2	3.9	0.348403 ± 1	1.8	0.7226	0.241578 ± 1	4.8	0.236450 ± 4	16.0
Serie 4												
JNdi-1 - Static	n=5	1.141807 ± 14	12.6	0.512095 ± 5	9.4	0.348400 ± 3	8.7	0.7222	0.241578 ± 4	15.2	0.236451 ± 5	19.1
JNdi-1 – Dyn 4L	n=7	1.141828 ± 5	4.6	0.512098 ± 2	3.6	0.3484028 ± 0.3	0.7	0.7224	0.241578 ± 1	5.1	0.236450 ± 4	15.9

Samarium		$^{144}Sm/^{152}Sm$	±	$^{147}Sm/^{152}Sm$	$^{148}Sm/^{152}Sm$	±	$^{149}Sm/^{152}Sm$	±	$^{150}Sm/^{152}Sm$	±	$^{154}Sm/^{152}Sm$	±
Serie 1												
Sm ICP	n=7	0.114978 ± 4	37.5	0.5647	0.420433 ± 8	17.9	0.516847 ± 6	10.9	0.275988 ± 7	26.9	0.850797 ± 11	13.5
Serie 2												
Sm ICP	n=8	0.114976 ± 4	31.2	-	0.420428 ± 6	14.8	0.516847 ± 2	4.1	0.275980 ± 3	9.7	0.850792 ± 9	10.4
Serie 3												
Sm ICP	n=5	0.114976 ± 2	19.9	-	0.420443 ± 4	10.3	0.516853 ± 5	9.6	0.275995 ± 7	27.1	0.850798 ± 22	25.4